# Total-Energy Distribution of Field-Emitted Electrons and Single-Plane Work Functions for Tungsten

L. W. SWANSON AND L. C. CROUSER
*Field Emission Corporation, McMinnville, Oregon*
(Received 27 March 1967)

Total-energy-distribution measurements in the temperature range 77 to 900°K along the ⟨310⟩, ⟨211⟩, ⟨111⟩, and ⟨611⟩ directions of W are in good agreement with the classical Fowler-Nordheim model for field emission. Work functions obtained from the $I(V)$ characteristics and energy-distribution results from these directions are reasonable. In contrast, energy-distribution results along the ⟨100⟩ and ⟨110⟩ directions do not agree with the free-electron model of Fowler and Nordheim nor do they yield sensible work-function values. Coating the emitter with a low-work-function Zr-O coadsorbate caused the ⟨100⟩ energy-distribution results to appear normal and yield sensible values of work function. Temperature coefficients of the work function for the ⟨110⟩, ⟨112⟩, ⟨100⟩, ⟨111⟩, ⟨116⟩, and ⟨310⟩ directions of clean W are −17.0, −14.3, −10.9, 3.5, 5.0, −3.2 ($\times 10^{-5}$)eV/deg, respectively. Upon coadsorbing Zr-O, the temperature coefficient of the ⟨100⟩ work function becomes negligible. The amplitude of low-frequency thermal-induced flicker noise was found to be least on the close-packed crystal faces. These results, when discussed in the light of the bulk band structure of W, indicate the plausibility of utilizing field-emission energy-distribution measurements to illustrate certain types of anisotropies in the energy surfaces of metals or semiconductors at or near the Fermi level.

## I. INTRODUCTION

FIELD electron emission from a metal into vacuum was treated theoretically in 1928 by Fowler and Nordheim[1,2] who based their calculations on a one-dimensional Sommerfeld free-electron model at 0°K. The resultant Fowler-Nordheim (FN) equation has since been found adequate for describing field electron emission from clean and adsorbate-coated metals at low temperatures. The FN equation was later modified to include temperature effects.[3–6] Although total-emission measurements generally confirmed the expected temperature and field dependence of the emitted electrons, a more rigorous test of the theory was performed by Young and Müller, who established both theoretically[7] and experimentally[8] the total-energy distribution of emitted electrons from a W substrate in the temperature range 77 to 300°K.

Thus, no serious experimental challenge of the adequacy of the original FN model has been made in the past. Recently, however, an investigation[9] of the energy exchange accompanying field electron emission over a wide temperature and field range revealed a significant departure from the predictions based on the Sommerfeld model, particularly at elevated temperatures. These results could be explained either by a departure of the total-energy distribution from theoretical expectations or by a large temperature coefficient of the average energy of the charge carriers in the bulk. In order to distinguish between these two possibilities, a detailed study of the total-energy distribution of field-emitted electrons from various crystallographic directions of a W emitter, as a function of temperature and in the presence of a coadsorbed zirconium-oxygen layer, has been performed. Although definite departures from the Sommerfeld free-electron model have been recently discovered along the ⟨100⟩ [10] and ⟨110⟩ [11] directions, the results of this study generally confirmed in the case of other directions, the expected temperature and field dependence of the total-energy distribution, at least for the range of temperature investigated (from 77°K to approximately 900°K).

Section II presents the derivation of the total-energy-distribution expression according to Stratton,[12] who included band-structure effects and the expected temperature and field effects; also discussed in Sec. II are the means by which single-crystal-face work functions can be determined from the energy-distribution measurements. Section III covers experimental methods and procedures and Sec. IV presents the calculated single-face work-function values and the experimentally determined variations of the local electric field strength with angular separation from the emitter apex. The temperature coefficient of the various single-face work functions is discussed in Sec. V. Section VI presents the total-energy-distribution measurements for several important directions of a clean W crystal. Section VII deals with the effect of a coadsorbed zirconium-oxygen layer on the energy distributions and work functions of the various crystal faces of a W emitter. In the light

[1] L. W. Nordheim, Proc. Roy. Soc. (London) **A121**, 626 (1928).
[2] R. H. Fowler and L. W. Nordheim, Proc. Roy. Soc. (London) **A119**, 173 (1928).
[3] A. Sommerfeld and H. Bethe, in *Handbuch der Physik*, edited by H. Geiger and Karl Scheel (Julius Springer, Verlag, Berlin, 1933), Vol. 24, p. 442.
[4] E. Guth and C. J. Mullin, Phys. Rev. **61**, 339 (1942).
[5] W. W. Dolan and W. P. Dyke, Phys. Rev. **95**, 327 (1954).
[6] E. L. Murphy and R. H. Good, Jr., Phys. Rev. **102**, 1464 (1956).
[7] R. D. Young, Phys. Rev. **113**, 110 (1959).
[8] R. D. Young and E. W. Müller, Phys. Rev. **113**, 115 (1959).
[9] L. W. Swanson, L. C. Crouser, and F. M. Charbonnier, Phys. Rev. **151**, 327 (1966).
[10] L. W. Swanson and L. C. Crouser, Phys. Rev. Letters **16**, 389 (1966).
[11] R. D. Young and H. E. Clark, Appl. Phys. Letters **9**, 265 (1966).
[12] R. Stratton, Phys. Rev. **135**, A794 (1964).

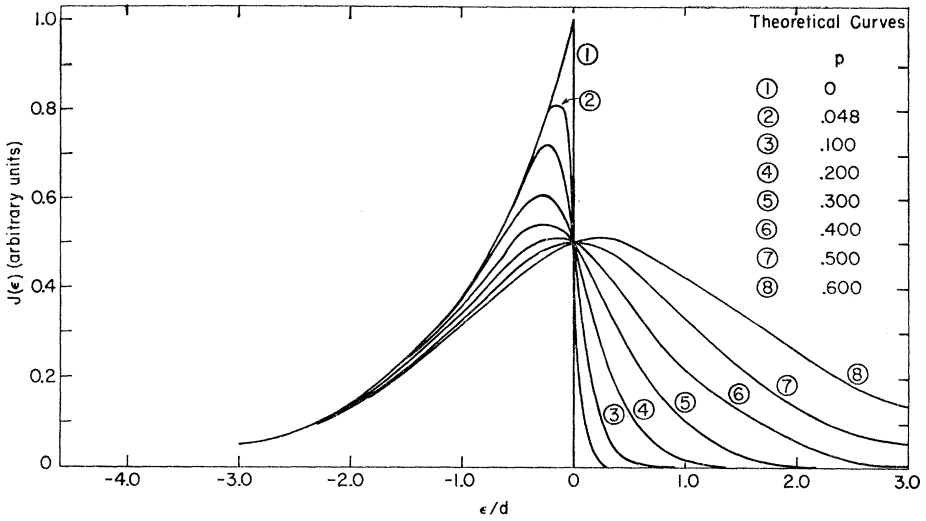


FIG. 1. Theoretical total-energy-distribution plots based on the free-electron model [Eq. (5)] at various values of $p$.

of these results, in Sec. VIII we discuss the applicability of the FN theory to metal substrates and speculate on the relation between band structure and some effects noted along the ⟨100⟩ and ⟨110⟩ directions.

## II. THEORETICAL CONSIDERATIONS

Since the original derivation of the FN equation several theoretical papers have expanded the original theory to include a broader range of temperatures,[6] normal- and total-energy distributions,[7] and, more recently, quantum-mechanical corrections to the one-dimensional image force model.[13] Because of the possibility that our results reveal band-structure effects, we shall use the derivation of the total-energy distribution by Stratton,[12] since it is applicable to a metal of arbitrary band structure. The study of the temperature dependence of the total-energy distribution requires careful consideration of the temperature dependence of the work function. Thus a short description of the analysis of the temperature dependence of work function by field-electron-emission techniques is also given.

### Total-Energy Distribution

An expression for the current density per unit total energy $J(\epsilon)$ (relative to the Fermi level $\epsilon=E-E_f$) was derived by Stratton[12] for a degenerate metal of arbitrary band structure and electron distribution $f(\epsilon)$ in momentum space. Employing the WKB approximation for the transmission coefficient, expanding in the usual fashion about $E_f$, and neglecting quadratic and higher-order terms, Stratton obtains

$$J(\epsilon)=J_0 f(\epsilon)e^{\epsilon/d}\left[1-\frac{1}{2\pi}\int_0^{2\pi}e^{-E_m/d}d\phi_p\right]\Big/ d, \quad (1)$$

where $J_0$ denotes the total current density (integrated over all $\epsilon$) at 0°K, which is related to the applied field $F$ and work function $\phi$ by

$$J_0=\frac{e^3F^2}{8\pi h\phi t^2(y)}\exp[-4(2m\phi^3)^{1/2}v(y)/3heF]$$
$$=\frac{1.54\times10^6F^2}{\phi t^2(y)}\exp[-6.83\times10^7\phi^{3/2}v(y)/F] \quad (2)$$

(the numerical form assumes $J_0$ in A/cm², $F$ in V/cm, and $\phi$ in eV), and where $E_m$ is the maximum value of the transverse energy $E_t$ for a specified energy surface $\epsilon$ and polar angle $\phi_p$ in the plane perpendicular to the emission direction. The value of $d$ is given by

$$d=heF/2(2m\phi)^{1/2}t(y)=9.76\times10^{-9}F/\phi^{1/2}t(y)\ \text{(eV)}. \quad (3)$$

The image correction terms $t(y)$ and $v(y)$ are slowly varying tabulated functions[14] of the auxiliary variable $y=(e^3F)^{1/2}/\phi$. As first shown by Fischer,[15] in the case of spherical energy surfaces with a positive Fermi energy and an effective mass $m_c=r_cm$ [so that $E_m(\epsilon,\phi_p)=r_cE$], Eq. (1) becomes

$$J(\epsilon)=J_0f(\epsilon)e^{\epsilon/d}\left[\frac{1-e^{-r_cE/d}}{d}\right]. \quad (4)$$

The specific effect of band structure occurs in Eqs. (1) and (4) only through the term in brackets and can be neglected when $E_m/d\gg1$. Under usual field-electron-emission conditions $d\cong0.15$ to 0.25 eV and for most degenerate metals exhibiting large Fermi energies $E_m$ is sufficiently large that the band-structure term in Eqs. (1) and (4) is negligible; however, for transition metals with partially filled narrow $d$ bands, the value of $E_m$ may be sufficiently small to perturb $J(\epsilon)$ through the band-structure term.

[13] P. H. Cutler and D. Nagy, Surface Sci. 3, 71 (1964).

[14] R. H. Good and E. W. Müller, in *Handbuch der Physik*, edited by S. Flügge (Springer-Verlag, Berlin, 1956), Vol. 21, p. 176.

[15] R. Fischer, Phys. Status Solidi 2, 1088 (1962); 2, 1466 (1962).

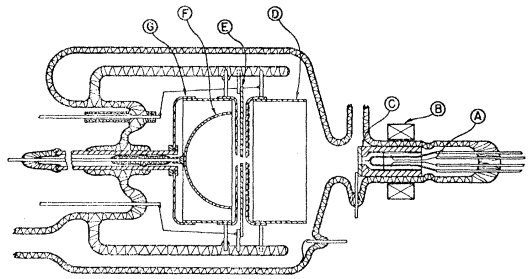


FIG. 2. Diagram of energy-analyzer tube utilized for measuring total-energy distributions at various temperatures.

The original derivation of $J(\epsilon)$ by Young,[7] based on the Sommerfeld free-electron model, is a special case of Eq. (1) when the Fermi-Dirac distribution of $f(\epsilon)$ is assumed and the band-structure term is neglected. With these considerations one obtains

$$J(\epsilon)=J_0 e^{\epsilon/d}/d(1+e^{\epsilon/pd}), \quad (5)$$

where $p=kT/d$ is a dimensionless parameter. The mathematical derivation of Eq. (5) breaks down for $p\geq 1$ and becomes unreliable when $p$ exceeds about 0.7. A graphical representation of $J(\epsilon)$ versus $\epsilon/d$ yields a set of curves whose shape depends only on the dimensionless parameter $p$ as shown in Fig. 1. The value $p=0.5$ leads to an exactly symmetrical distribution of the emitted electrons about $E_f$; the condition $p=0.5$ occurs when the temperature is equal to an "inversion temperature" $T^*$:

$$T^*=d/2k=5.67\times 10^{-5}F/\phi^{1/2}t(y) \quad (^\circ\text{K}). \quad (6)$$

The physical significance of this inversion temperature was discussed in an earlier publication.[9]

Integration of Eq. (5) over $\epsilon$ yields the well-known expression for thermal-field (TF) emission $J_{TF}$:

$$J_{TF}=J_0\int_{-\infty}^{\infty}\frac{e^{\epsilon/d}}{d}[1+e^{\epsilon/pd}]^{-1}\,d\epsilon=J_0\pi p/\sin\pi p, \quad (7)$$

which is valid in the range $0\leqslant p<0.7$. For small values of $T$, we note $\pi p/\sin\pi p\cong 1$ and the 0°K approximation $J=J_0$ is obtained as given in Eq. (2).

### Work-Function Measurements

Energy-distribution measurements can be combined with current-voltage $I(V)$ data to yield assumption-free work functions of single-crystal faces.[16] The ability to perform such an analysis depends on the validity of the total-energy-distribution expression Eq. (5). For retarding potential-energy analyzers the emitted electrons can be collected at a metal surface of work function $\phi_c$ only if their total energy $E$ exceeds

$$E>\phi_c+E_f-V_t, \quad (8)$$

where $V_t$ is the emitter to collector bias potential; thus, increasing $V_t$ allows all electrons emitted down to a certain energy level $\epsilon=\phi_c-V_t$ to be collected. At 0°K the condition $V_t=\phi_c$ represents the current cutoff since electronic states above $E_f$ are not populated, and the total collected current $I_p$ at a specified value of $\epsilon$ is given by

$$I_p=\frac{I_0}{d}\int_0^{-\epsilon}e^{\epsilon/d}d\epsilon=I_0(1-e^{-\epsilon/d}), \quad (9)$$

where $I_0$ is the maximum field electron current. By rewriting Eq. (9) in the working form

$$\log_{10}(I_0-I_p)/I_0=\frac{-\phi_c}{2.3d}+V_t/2.3d, \quad (10)$$

it is clear that the values of $d$ and $\phi_c$ can be obtained, respectively, from the slope $m_e$ and the intercept of a plot of $\log_{10}(I_0-I_p)/I_0$ versus $V_t$. The experimental value of $d$ so obtained can be compared with that obtained by Eq. (3) in order to provide a rough check on the energy-distribution theory.

It is further observed from Eq. (2) that a "Fowler-Nordheim plot" of $\log_{10}I_0/V^2$ versus $1/V$ yields a slope $m_f$ which is related to $\phi$ and the geometric factor $\beta=F/V$ as follows:

$$m_f=-2.96\times 10^7\phi_f^{3/2}s(y)/\beta \text{ (cm)}, \quad (11)$$

where $s(y)$ is a slowly varying tabulated function[14] arising from the image potential. The values of $\phi_f$ relative to a reference value $\phi_0$ can readily be established as shown by rewriting Eq. (11) as follows:

$$\phi_f=\phi_0(m_f/m_{f0})^{2/3}, \quad (12)$$

where $m_{f0}$ is the FN plot slope for the reference surface and the value $\beta$ is assumed unchanged. Because of the difficulty in determining accurate values of $\beta$, Eq. (11) cannot be employed for an accurate work-function calculation. However, as pointed out by Young,[11] Eqs. (10) and (11) can be combined to give the following expression for $\phi$:

$$\phi_e=-3m_f t(y)/2m_e V s(y), \quad (13)$$

where $V$ is the anode voltage. Accordingly, a value of work function can be ascertained from combined energy-distribution and FN plots via Eq. (13) which eliminates assumptions concerning $\phi_0$ and $\beta$.

Recent anomalous values of $\phi_e$ calculated by the above method have motivated a reexamination[16] of Eq. (13) and the inclusion of surface patch-field effects. This consideration led to a correction term which multiplies the right-hand sides of Eqs. (12) and (13) by factors $(\pm F_0/\beta V+1)^{4/3}$ and $(\pm F_0/\beta V+1)$, respectively, where $F_0$, the net strength of the patch field, is positive for a high $\phi$ plane and negative for a low $\phi$ plane relative to the surrounding planes. It was shown that a crystal

[16] R. D. Young and H. E. Clark, Phys. Rev. Letters **17**, 351 (1966).

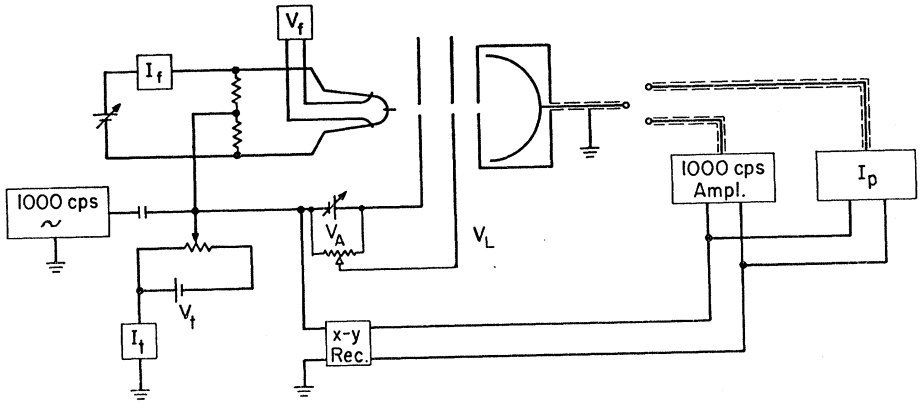


FIG. 3. Circuit diagram for energy-analyzer tube.

plane 400 Å in diam possessing a work-function difference between it and the surroundings of 0.5 eV would introduce a patch-field correction of about 0.1 eV in Eq. (12). The significance of patch-field corrections will be discussed in a later section.

### Temperature Dependence of the Work Function

In order to assess the effect of temperature on the energy-distribution results it is necessary to evaluate and understand the variation of the local work function with temperature. A thorough review of the theoretically expected contributions to the temperature coefficient of the work function has been given by Herring and Nichols[17] and experimentally confirmed by both contact-potential[18] and field-electron-emission[19] methods. Using field electron emission, van Oostrom[19] measured values of $d\phi/dT$ by monitoring the change in field-electron current at constant voltage between 78 and 293°K. A more accurate and less restrictive method described here involves obtaining FN plots at each temperature. Using the more general TF formulation given in Eq. (7), the 0°K expression for $m_f$ given in Eq. (11) becomes

$$m_f = V(1-\pi p \cot\pi p)/2.3 - 2.96\times10^7\phi^{3/2}s(y)/\beta. \quad (14)$$

When the correction term $\delta = V(1-\pi p \cot\pi p)/2.3$ cannot be neglected, the work function at temperature $T$ becomes

$$\phi(T) = \phi_0\left(\frac{m_f+\delta}{m_{f0}}\right)^{2/3}\left(\frac{\beta(T)}{\beta_0}\right)^{2/3}, \quad (15)$$

where the subscript 0 refers to the low-temperature values, and $\beta(T)$ corrects for the thermal expansion of the emitter of radius $r$ and is approximately given by

$$\beta(T) = \beta_0(1-\Delta r/r). \quad (16)$$

Thus, field-electron $I(V)$ data can be utilized to evaluate the temperature coefficient of work function over the temperature range of validity for Eq. (7). In practice, the upper limit of temperature is determined by the threshold of field-induced rearrangement of the emitter geometry due to surface migration, which, in most cases, occurs below the temperature where Eq. (7) ceases to be valid. The value of $V$ midrange in the FN plot is used for convenience in the correction term $\delta$.

## III. EXPERIMENTAL TECHNIQUES AND PROCEDURES

The energy-analyzer tube utilized in this investigation was based on a design by van Oostrom of the Phillips Laboratory[20] and is depicted in Fig. 2. Briefly, the tube is designed in such a way that electrons passing through the lens system are focused near the center of the spherical collector F. The electrode system of the analyzer consists of an anode D, a focusing electrode E, and a Faraday cage G. The latter electrode is operated near ground potential and acts as a shielding electrode for the hemispherical collector (also operated near ground potential) and accordingly reduces the effect of undesirable reflection inherent in most retarding potential analyzers. It should be noted that electron trajectories pass through a crossover formed near the center of the hemispherical collector and have nearly normal incidence on the collector surface so that the total energy of the emitted electrons will be analyzed.

The tube, constructed of aluminosilicate glass, contained molybdenum electrodes and a collector consisting of a hot-spin molybdenum hemispherical cup (radius of curvature of 15 mm) exhibiting a surface roughness less than 1$\mu$. The electrode apertures were 1, 2, and 4 mm, increasing in size toward the collector. A thin Willemite screen on the anode allowed pattern viewing. Deposition of coadsorbed zirconium-oxygen was accomplished by resistively heating a poorly outgassed 10-mil zirconium wire contained in the tubulation

[17] C. Herring and M. H. Nichols, Rev. Mod. Phys. **21**, 185 (1949).
[18] C. R. Crowell and R. A. Armstrong, Phys. Rev. **114**, 1500 (1959).
[19] A. van Oostrom, Phys. Letters **4**, 34 (1963).
[20] A. van Oostrom, Philips Res. Rept. Suppl. (Netherlands) **11**, 102 (1966).

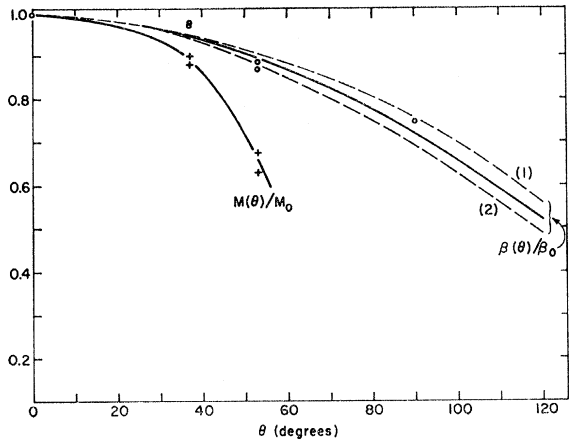


FIG. 4. $\beta(\theta)/\beta_0$ is the relative variation of electric field with angular distance from emitter apex, $\theta$. Dashed curves: (1) emitter with pronounced constriction; (2) emitter with slight constriction; solid line for average emitter shape (see Ref. 23). Experimental data for $\beta(\theta)/\beta_0$ given by circles. Lower curve gives the relative variation of magnification with $\theta$; data points indicated by crosses.

opposite the emitter. Inserting the tube in liquid nitrogen greatly increased the vacuum stability, reduced tip contamination from the screen to a negligible amount during the emission of high total currents (2 $\mu$A), and extended the lower limit of the temperature range to 77°K.

In practice, the anode potential $V_A$ was constant and the focal length adjusted by varying the potential of the lens electrode $V_L$ (see Fig. 3). The total-energy-distribution curves were taken for fixed values of $V_L$ and $V_A$ by varying the cathode potential approximately 1.5 V. The ratio of $V_L$ to $V_A$ is a critical quantity and for this particular lens system best results were obtained with $V_L/V_A=0.003$.

The emitter assembly A consisted of a field-emission tip spot-welded to a 10-mil tungsten filament with 3-mil potential leads utilized to sample the potential $V_f$ and, hence, resistance change across a small length of filament in order to accurately measure the emitter temperature. The temperature of the emitter was controlled by resistively heating the emitter support filament with an isolated dc supply as shown in the diagram of Fig. 3. Care was taken to insure that $I_fR$ drops across the filament during heating would not alter the tip bias voltage by applying $V_t$ at the center of a 50-Ω resistor symmetrically placed in the circuit as shown.

The aperturing of the primary beam by the 1-mm probe hole was sufficient to cause a ratio of the collected to the total emitted current of $\sim 10^{-3}$ when probing the emission from a low-work-function region of the emitter. This corresponds to a tip area seen by the probe hole of approximately $3\times10^{-14}$ cm$^2$ for the emitter sizes employed in this investigation. The collector current $I_p$, which ranged from $10^{-9}$ to $10^{-14}$ A, was measured by a Cary vibrating-reed electrometer with an $xy$ recorder readout. The energy-distribution curves were obtained by graphical or electronic differentiation of the collector current $I_p$ versus tip bias voltage $V_t$ curves. In order to electronically differentiate the integral curves, $I_p$ was modulated by a 15-mV, 1000-cps signal superimposed on the emitter bias voltage and detected with a narrow-band 1000-cps amplifier. The magnitude of the 1000-cps signal in the collector circuit was proportional to the first derivative of $I_p$ with respect to $V_t$ and was also plotted on an $xy$ recorder as a function of $V_t$.

A small, rotatable external electromagnet B and internal concentrator C shown in Fig. 2 were used to deflect the beam in order to position the emission from the desired crystallographic plane onto the aperture of the anode electrode. The internal concentrator could be tied electrically to the anode potential by allowing it to rest on a small platinum ring. With this arrangement, the tube could be used to measure both energy distribution and work function from various single-crystal faces. The $I(V)$ data for work-function measurements were obtained with the tip at $-8$ V and a constant ratio of $V_L/V_A$ in order that the electron trajectories through the lens would be constant over the voltage range. During the $I(V)$ measurements with magnetic deflection, compensation of the magnetic current must be performed in order to maintain a constant position of the desired crystal face on the aperture. Work-function and energy-distribution measurements were taken along a particular zone line at positions where the current went through either a maximum or minimum as a function of beam deflection. This allowed precise positioning of the desired crystal face on the aperture of the anode throughout the voltage range covered by the FN plot. The total current $I_t$ was measured simultaneously with the probe current as shown schematically in Fig. 3.

The resolution of a retarding potential analyzer tube estimated by van Oostrom[20] to be 10 mV for this design, is customarily ascertained by comparison of the experimental and theoretical energy-distribution curves at very low temperatures, as this experimental method is simpler and more reliable than a rigorous analysis and calculation of all factors leading to the resolution limit. Magnetic shielding placed around the tube reduced the earth magnetic field to zero; however, a fringing magnetic field was present in the region of the collector when beam deflection was used to examine an off-axis plane, reaching a value of approximately 0.1 G at a beam deflection of 55°. The effect of this magnetic field on the resolution, though not calculated precisely, was thought to be small for this tube design. A more serious effect on the measured energy distribution in this analyzer design is caused by the alteration of the electron optics as the apparent electron source and, hence, the position of the crossover changes with beam deflection. The seriousness of this effect will be discussed later in connection with the results. In order to minimize magnetic deflection, the emitter orientation was

TABLE I. Results from clean tungsten substrates ⟨310⟩-oriented emitter.

| Plane | $V$ (V) | $d$ (eV) | $\phi_e$ (eV)[a] | $\phi_f$ (eV)[a] | $\beta/\bar{\beta}(\theta)$ | $M\times10^{-5}$ | $\theta$ (deg) |
|---|---|---|---|---|---|---|---|
| 211 (flashed) | 1234 | 0.135 | 4.84±0.06 | 4.93±0.01 | 0.97 | 2.1 | 25 |
| 211 (annealed) | 1234 | 0.148 | 5.05±0.05 | 5.00±0.02 | 1.01 | 2.7 | 25 |
| 310 (flashed) | 1234 | 0.149 | 4.34±0.02 | 4.21±0.01 | 1.05 | 3.6 | 0 |
| 310 (annealed) | 1234 | 0.147 | 4.16±0.03 | 4.28±0.01 | 0.96 | 3.4 | 0 |
| 111 (annealed) | 1306 | 0.154 | 4.80±0.03 | 4.49±0.02 | 1.11 | 1.6 | 43 |
| 110 (annealed) | 1517 | 0.193 | 6.20±0.06 | 5.02±0.03 | 1.37 | 2.2 | 26 |
| 100 (annealed) | 1221 | ··· | ··· | 4.59±0.02 | ··· | 1.5 | 18 |
| | | | ⟨100⟩-oriented emitter | | | | |
| 611 (annealed) | 1461 | 0.141 | 4.41±0.04 | 4.32±0.04 | 1.03 | 1.8 | 13 |
| 110 (annealed) | 1990 | ··· | ··· | 5.15±0.05 | ··· | 2.6 | 45 |
| | | | ⟨110⟩-oriented emitter | | | | |
| 110 (annealed) | 1773 | 0.177 | 6.40±0.09 | 5.79±0.04 | 1.16 | 1.4 | 0 |
| 110 (~4° off axis annealed) | 1701 | 0.185 | 6.02±0.06 | 5.16±0.02 | 1.26 | 2.3 | ~4 |

[a] Uncertainties refer to probable error obtained from a least-squares analysis of the data.

varied by fabricating emitters from zone-refined oriented W wires produced in this laboratory. For this study ⟨310⟩, ⟨110⟩, and ⟨100⟩ emitter orientations were employed, reducing to 35° the maximum deflection required for examination of any crystal orientation.

In the present case the resolution for planes 13° to 26° off the emitter axis ranged from 30 to 40 mV with poorest resolution at the largest beam deflection as expected. For an on-axis direction the resolution was considerably better, but not as good as the 10-mV value claimed by van Oostrom. Inasmuch as resolution is not critical, except at very low temperatures where a sharp peak occurs near the Fermi energy, the resolution at maximum beam deflection was considered adequate to investigate the energy-distribution shapes at elevated temperatures.

## IV. SINGLE-PLANE WORK FUNCTIONS

The variation of $\beta$ (i.e., of local electric field at a given applied voltage) with angular separation $\theta$ from the emitter apex is one of the primary difficulties in utilizing Eq. (12) to obtain meaningful results on the variation of relative work function with crystal direction. This variation in $\beta$ is due primarily to the increased shielding of the tip by the emitter shank, which causes a monotonic decrease in $\beta$ with increasing $\theta$. In addition, another variation in $\beta$ occurs due to differing amounts of the thermodynamically motivated local faceting of certain crystal faces.[21] This local faceting varies in magnitude with the temperature at which the emitter was annealed prior to thermal quenching, and is largest for the low-index planes because of their lower surface energy. The slight effect of annealing temperature on the value of $\phi_f$ derived from Eq. (12) for a given plane, first noticed by Müller,[22] is caused at least in part by this temperature-dependent local faceting.

To allow correction of the first problem we have established experimentally the variation in $\beta$ with $\theta$ by measuring the relative variation in $m_f$ for various {310} planes along the [100] zone line of a ⟨310⟩ oriented emitter. If the reasonable assumption that each 310 plane exhibits identical values of $\phi$ is accepted, then the relative variation of $\beta$ with $\theta$ can be obtained from $m_f$. The relative values of $\beta$ measured for the ⟨310⟩, ⟨130⟩, ⟨$\bar{3}$10⟩, and ⟨$\bar{1}$30⟩ directions are shown in Fig. 4, where $\beta_0$ refers to the on-axis value. The data points fall within the limits established by an analytical calculation[23] of $\beta/\beta_0$ for two sphere-on-orthogonal cone models imitating two emitter profiles with a slight and a pronounced constriction. The deviation of the data from the solid curve representing an average emitter shape does not exceed 2%, which is within the accuracy of the FN plots. It is therefore concluded that the corrections to the probe FN work-function calculations, based on the average emitter shape curve of Fig. 4, are reasonably accurate. Thus, one of the major sources of error of the FN slope method of determining $\phi_f$ for various crystal faces is removed.

Also plotted in Fig. 4 is the variation of linear magnification $M$ versus $\theta$ which is related to the probe hole area $A_p$ and the emitter area $A$ "seen" by the probe hole as follows:

$$M=(A_p/A)^{1/2}. \tag{17}$$

The emitting area can be obtained directly from the experimental intercepts $B(\theta)$ of the FN plots by noting

$$B(\theta)=CA\beta^2/\phi, \tag{18}$$

where $C$ is a constant; whence, according to Eqs. (17) and (18), the value of $M$ at an angle $\theta$ from the emitter apex relative to the magnification $M_0$ along the emitter axis is given by

$$M(\theta)/M_0=[B_0/B(\theta)]^{1/2}\beta(\theta)/\beta_0. \tag{19}$$

The values of $M(\theta)/M_0$ in Fig. 4 decrease more rapidly

[21] M. Drechsler and H. Liepack, *Adsorption et Croissance Cristalline* (Centre National de la Recherche Scientifique, Paris, 1965), p. 1.

[22] E. W. Müller, J. Appl. Phys. **26**, 732 (1955).

[23] W. P. Dyke *et al.*, J. Appl. Phys. **24**, 570 (1953).

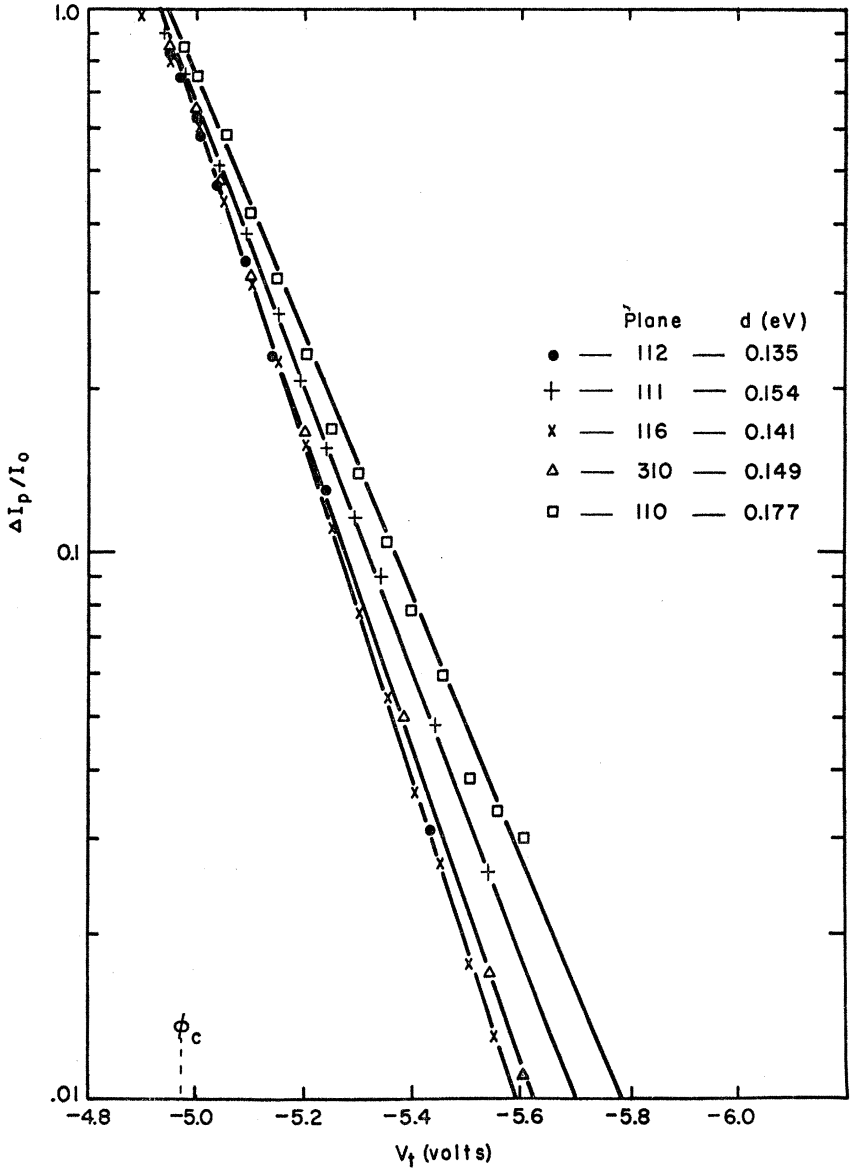


FIG. 5. Typical results of the integral field-emission current plotted according to Eq. (10) from various directions of a clean W emitter at 77°K. The values of $d$ listed in Table I are obtained from the slope of such plots. Collector work function $\phi_c$ is obtained from the intercept on the abscissa axis at $\Delta I_p/I_0=1$.

with $\theta$ than $\beta(\theta)/\beta_0$, as expected from the enhanced beam compression caused by the emitter shank, although the exact functional form of the relation $M=f(\beta)$ cannot be established because of possible distortion of the beam by the deflecting magnetic field, particularly at large $\theta$.

The values of work function $\phi_f$ given in Table I for the various crystal faces were obtained from Eq. (12) by using the average value $\phi_0=\bar{\phi}_f=4.52$ eV as the reference and making the appropriate corrections in $\bar{\phi}_f$ for variations in $\beta(\theta)$ as given in Fig. 4. Prior to each measurement the emitter was either annealed for 300 sec at 1000°K or flashed to 1800°K and quenched to 77°K at which temperature each of the measurements was made. The results show that the annealed values of $\phi_f$ for the (211) and (310) planes are slightly larger than those obtained by flashing and quenching because of alteration of the end form or local work function with temperature.

The values of $M$ given in Table I have been corrected for the variation in $\bar{\beta}$ as emitters of differing radii of curvature $r$ were used. This was accomplished by assuming that $M \propto \bar{\beta} \propto 1/r$ so that uncorrected $M$ values could be multiplied by $\bar{\beta}_0/\bar{\beta}$, where $\bar{\beta}_0$ was an arbitrarily chosen reference. From Table I we observe that the local value of $M$ decreases in the order 310>211>611 >111>100>110, provided the ⟨110⟩ results are accepted for the (110) plane. This is nearly identical to the order observed in a similar study by van Oostrom,[20] except for the higher relative value of $M_{110}$ observed here. Inspection of thermally annealed field-ion micro-

graphs by Bassett[24] showed that the (110) and (211) planes possess equally large facets, yet both van Oostrom's and our results show $M_{211}>M_{110}$. This implies that local values of $M$ are influenced by the surrounding equipotential surface or by possible transverse electric fields due to patch effects. Somewhat surprising is the low relative value of $M_{100}$, since field-ion micrographs indicate that (211) net planes are much larger than the (100) planes, thereby suggesting $M_{100}>M_{211}$. As shown earlier,[10] the Sommerfeld model upon which the FN theory is based does not hold for the ⟨100⟩ direction of clean W; hence it is possible that the form of the FN equation pre-exponential, from which $M_{100}$ is evaluated, is incorrect.

An interesting feature of the Table I results is the low value of the (110) work function for non-⟨110⟩-oriented emitters; both ⟨310⟩- and ⟨100⟩-oriented emitters gave nearly identical values of $\phi_f \cong 5.0$ eV for the (110) plane. On the other hand, the ⟨110⟩-oriented emitter gave the usual 5.8-eV value of $\phi_f$ for the (110) plane. This effect of emitter orientation on $\phi_f$ was confined to the (110) plane, since all other planes gave nearly identical values of $\phi_f$ independent of emitter orientation after corrections for the $\beta(\theta)$ variation were made. We have no clear-cut explanation for these orientational effects on the value of $\phi_f$ for the (110) plane, although in comparing the (110) results from the ⟨310⟩-oriented emitter with the 4° off-axis results from the ⟨110⟩-oriented emitter, one observes similar values of $M$ and $\phi_f$. This suggests that proper alignment of the (110) plane by magnetic deflection is somehow impossible for non-⟨110⟩-oriented emitters. For the ⟨110⟩-oriented emitter the value of $M$ is lowest for the center of the (110) plane and increases slightly toward the net plane edges, as expected in view of the pronounced faceting of this plane.

Given in column 4 of Table I are work-function values $\phi_e$ calculated according to Eq. (13) employing slope values $m_e$ from plots of $\Delta I_p/I_0$ versus $V_t$; selected such plots are shown in Fig. 5. The ratios of local $\beta$ to average[25] $\bar{\beta}(\theta)$ were obtained from the ratios $(\phi_e/\phi_f)^{3/2}$. Values of $\phi_e$ and $\phi_f$ for the (211) plane agree within experimental error indicating no large discrepancy between $\beta_{211}$ and $\bar{\beta}(\theta)$ for both flashed and annealed end forms. The (310) results show a slight lowering of $\beta_{310}$ and $\phi_e$ on annealing, the latter being contrary to the expectation that removal of quenched-in atomic disorder by annealing should lead to a higher value of work function. Examination of thermally annealed patterns suggests that $\beta_{111}/\bar{\beta}(\theta)$ should be less than unity, rather than larger by 11%. It is believed that electron optical effects due to the large angular deflection (see column 8, Table I) of the beam may have increased the measured value of $\phi_e$ for the (111) plane. This belief was substantiated by noting that the value of $\phi_e$

[24] D. W. Bassett, Proc. Roy. Soc. (London) 286, 191 (1965).

[25] $\beta(\theta)$ refers to the average value of $\beta$, but modified by the field reduction with $\theta$ according to Fig. 4.

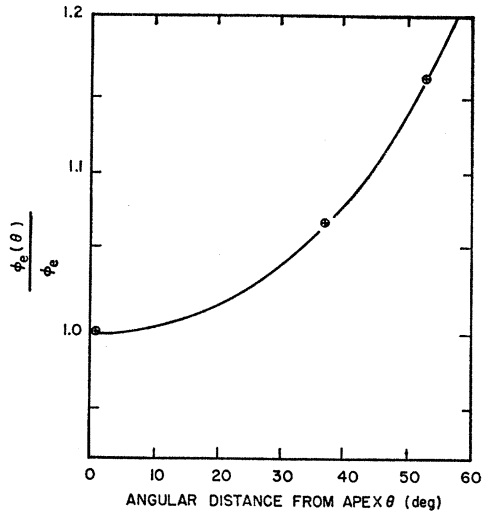


FIG. 6. Relative variation of absolute work function [calculated by Eq. (13)] with angular distance from apex for various {310} planes along the [100] zone line of a W emitter.

calculated for various {310} planes increased with $\theta$ as shown in Fig. 6. The values of $\phi_e$ given in Table I have been corrected by assuming the apparent increase in $\phi_e$ with $\theta$ shown in Fig. 6 for the {310} planes applies to others as well. Excluding the (111) results, this correction was less than 3% for all planes listed in Table I.

As a further check on the free-electron theory of field emission along the ⟨310⟩ direction, values of $\phi_e$ were determined according to Eq. (13) for a range of anode voltages. The results, given in Table II, yield a value of $\phi_e=4.40\pm0.13$ eV for the ⟨310⟩ direction compared to a value of $\phi_f=4.32\pm0.05$ eV. The close agreement between values of $\phi_e$ evaluated at different anode voltages provides further support for the validity of the Sommerfeld model in describing emission along the ⟨310⟩ direction. Also, the close agreement between $\phi_e$ and $\phi_f$ suggests that $\beta_{310}\cong\bar{\beta}$ for the (310) plane. The latter result is not unexpected since the (310) plane of W appears to be relatively small and free from faceting in its thermal end form.[24]

For the most part, local variations in $\beta$ with crystallographic direction do not follow the variations in $M$ for clean annealed W. The large value of $\phi_e$ relative to $\phi_f$ given in Table I for the off-axis (110) plane leads to a value of $\beta_{110}/\bar{\beta}(\theta)$ which is unusually high in view of the

TABLE II. Values of $\phi_e$ for (310) plane as a function of anode voltage, where $\phi_f=4.32\pm0.05$ eV.

| $V$ (V) | $\phi_e$ (eV) |
|---|---|
| 1461 | 4.42 |
| 1391 | 4.47 |
| 1299 | 4.32 |
| 1228 | 4.33 |
| 1158 | 4.42 |
| 1067 | 4.44 |

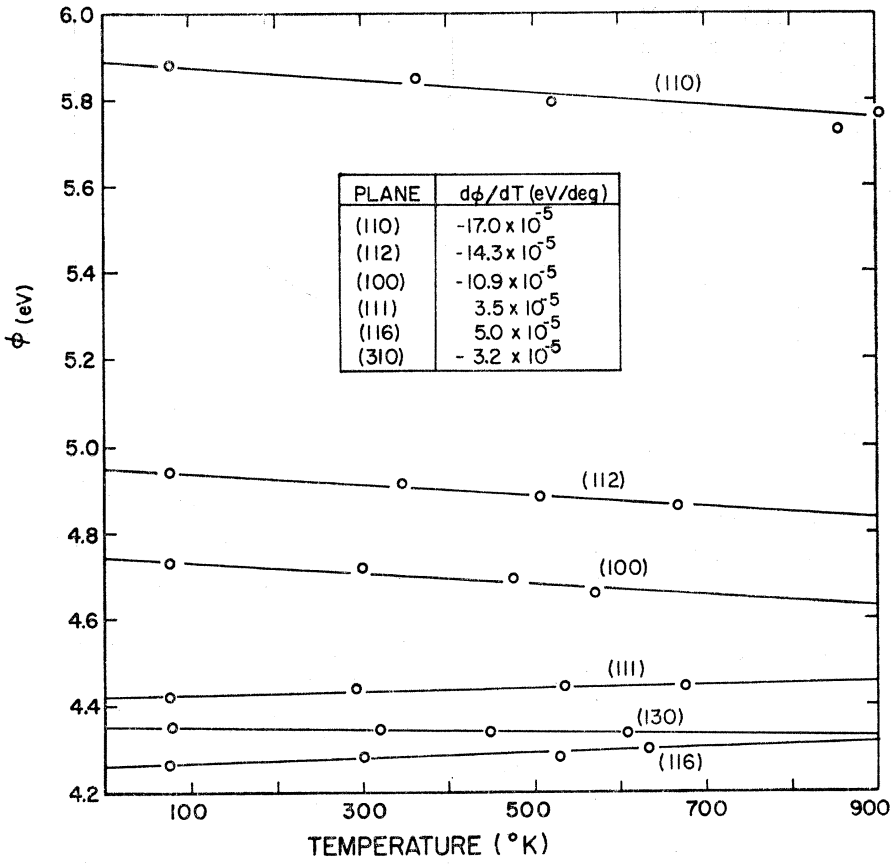


FIG. 7. Temperature dependence of work function for various planes of a clean W substrate as determined from field-electron-emission data.

low value of $M$ and the well-known faceted end form of this plane. A closer agreement between $\phi_f$ and $\phi_e$ is obtained for the (110) plane of the ⟨110⟩-oriented emitter; however, it is still anomalous in that $\beta_{110}/\bar{\beta}(\theta)$ is expected to be less than unity for the faceted (110) planes. It should be pointed out that the (110) value of $\phi_e$ for the ⟨110⟩-oriented emitter listed in Table I was the lowest obtained; other measurements of $\phi_e$ for the (110) from non-⟨110⟩-oriented emitters were even larger (in excess of 7 eV in a few cases) and seemed to vary in an erratic fashion with the annealing history of the emitter as also observed by Young.[11] In view of the erratic nature of the (110) results no accurate value of its work function can be given from this work. On the other hand, values of $\phi_f$ for all other planes given in Table I should be accurate to within the $\sim\pm 2\%$ uncertainty of the field falloff shown in Fig. 4.

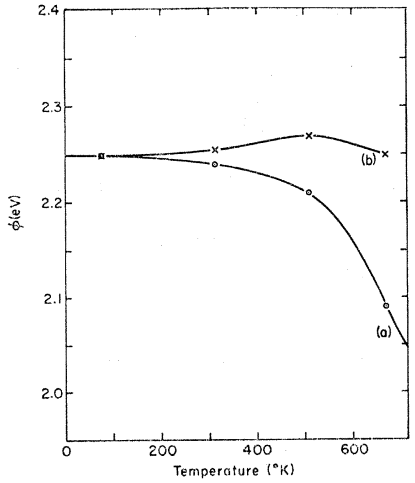


FIG. 8. Curve (a) is the variation of the apparent work function of the (100) plane of a Zr-O coated tungsten emitter as determined by Eq. (12). Curve (b) gives the curve (a) results corrected for the TF contribution to the field emission current according to Eq. (15).

As pointed out by Young,[16] patch-field corrections can be important for field-emission measurement of work function on a plane possessing a large work-function difference from its surroundings as in the case of the (110) of a bcc crystal. Unfortunately, as outlined by Young, the patch-field corrections cause both $\phi_e$ and $\phi_f$ for the (110) to increase. In view of the fact that work-function measurements of macroscopic (110) surfaces by all other methods give values in the range of 5.0 to 5.3 eV, we find it difficult at this time to accept values in excess of the $\sim$6.0 eV value as given here and elsewhere[22] by Fowler-Nordheim slope methods. This difference of nearly 1 eV between field-emission and

TABLE III. Comparison of the flicker noise for various planes at ~500°K.

| Plane | Atom density ($\times 10^{14}$ atoms/cm$^2$) | $\Delta I/I_p$ |
|---|---|---|
| 110 | 14.14 | 0 |
| 100 | 10.00 | 0.011 |
| 211 | 8.16 | 0.024 |
| 310 | 6.32 | 0.083 |
| 111 | 5.77 | 0.026 |
| 611 | 3.20 | 0.028 |
| 100 (with Zr-O) | ··· | 0.006 |

non-field-emission methods of measuring the (110) work function may be due to the more nearly ideal surface obtained by field-emission methods as dramatically established by field-ion micrographs.[24] It is conceivable that patch-field corrections enter more subtly than was outlined by Young. For example, the transverse fields arising from patch effects may affect the electron tunneling in a fashion not obvious from the usual one-dimensional models. Also, the perturbation of electron trajectories by the combined applied and transverse patch fields can alter $J$ so as to compensate for the change in $m_f$. As will be discussed more fully in a later section, band-structure effects, which are manifest in the ⟨100⟩-direction results and therefore disallow the calculation of $\phi_e$, may also exist and thus obviate the strict use of the Sommerfeld model along the ⟨110⟩ direction.

## V. EFFECT OF TEMPERATURE ON EMISSION

The variation of $\phi_f$ with temperature for several major directions of clean and coated W has been measured by the field-emission methods described in Sec. II. The results, shown in Fig. 7 for clean W and Fig. 8 for Zr-O coadsorbed on W, have several surprising and interesting features. The validity of these results is based on the applicability of the Sommerfeld and the one-dimensional image potential model for describing field emission from W. As will be shown later, this model, though obviously inadequate for the ⟨100⟩ and possibly ⟨110⟩ directions of clean W, appears to be adequate for all other major crystal directions investigated. To what extent the $\phi_f$-versus-$T$ results for these planes might be affected by the inadequacy of this model is not yet clear. Before discussing the temperature coefficient of work function, we shall mention briefly a related phenomenon which caused some difficulty in obtaining energy distributions at elevated temperature.

### Flicker Noise

Work-function and energy-distribution measurements were limited to temperatures below that required to cause gross thermodynamically motivated geometric changes[26] in the emitter surface. This upper limit was

[26] P. C. Bettler and F. M. Charbonnier, Phys. Rev. 119, 85 (1960).

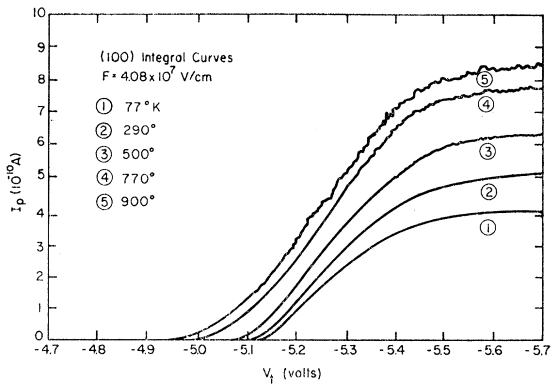


FIG. 9. Recorder plots of the probe current $I_p$ as a function of emitter bias voltage $V_t$ at various temperatures.

approximately 900°K for the thermally annealed emitters employed here, whose radii of curvature exceeded 1500 Å. However, minor atom motion occurs well below this temperature, e.g., lateral displacement of exposed surface atoms on a net plane occurs at temperatures as low as 300°K,[27] whereas gross surface geometric changes of a field evaporated end form do not occur below ~500°K.[24] This has been confirmed by observing the onset of flicker noise in the probe current with increasing temperature as shown in Fig. 9 for the ⟨100⟩ direction. Flicker noise, which is proportional to $I_p$, stems from fluctuations in the local surface potential due to thermal initiated atomic displacements which result in a low-frequency modulation of $I_p$. We estimate that the probe hole accepts emission from ~30 surface atoms for the emitter size employed; hence statistical fluctuations involving relatively few atoms can lead to the noise shown in Fig. 9.

As other planes were investigated it was observed that the onset of flicker noise generally occurred at increasingly higher temperature for the more densely packed planes. By measuring the average amplitude $\Delta I$ of the flicker noise at some value of $I_p$, one may use the ratio $\Delta I/I_p$ for various crystal directions at a specified temperature as a rough comparison of the ease of thermally exciting the surface atoms. The results shown in Table III indicate an inverse relationship between low-frequency flicker noise (less than 10 cps for the recorder employed) and the atom density of the emitting plane. The (310) plane is an interesting exception in that it exhibits considerably more flicker noise than other planes investigated. Excluding the latter exception, the data suggests that the thermal initiated atomic displacement in the central region of a net plane is diminished as the number of next nearest neighbors increase.

Flicker noise was greatly increased by the presence of a small amount of gas contamination and could be used as a sensitive criterion of the surface cleanliness.

[27] G. Erlich and F. G. Hudda, J. Chem. Phys. 44, 1039 (1966).

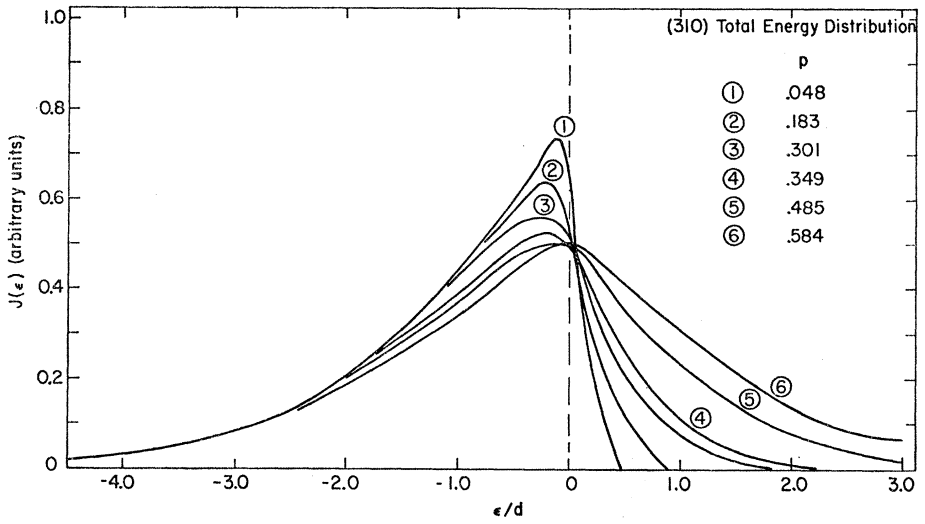


FIG. 10. Experimental total-energy-distribution plots along the ⟨310⟩ direction of a W emitter as a function of $p$, where $d=0.137$ eV and $F=3.06\times10^7$ V/cm.

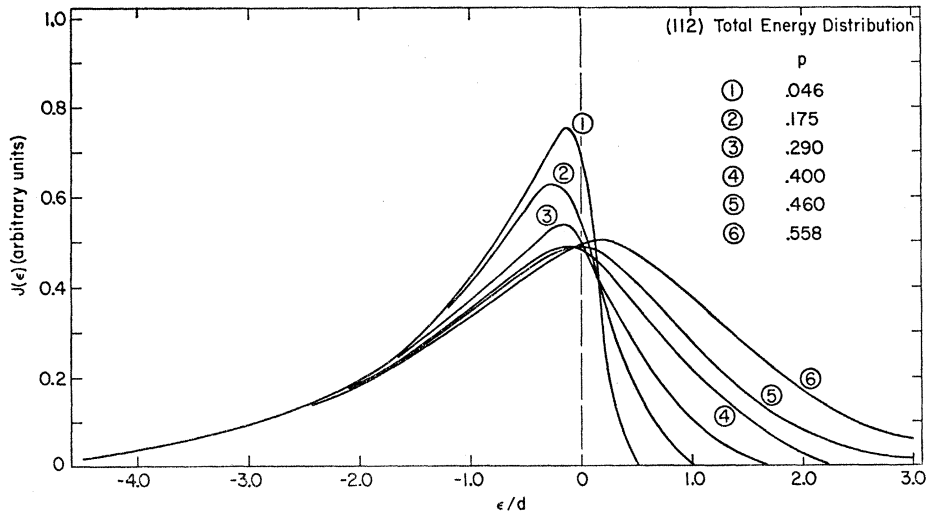


FIG. 11. Experimental total-energy-distribution plots along the ⟨112⟩ direction of a W emitter as a function of $p$, where $d=0.146$ eV and $F=3.48\times10^7$ V/cm.

An interesting exception, however, was the low work-function coadsorbed Zr-O layer on the (100) plane of W which actually reduced flicker noise.

### Temperature Coefficient of Single-Plane Work Functions

Perhaps the most interesting feature of the temperature coefficient of work function as depicted in Fig. 7 for clean W is its variation in both sign and magnitude with crystal direction. Over the temperature range investigated the temperature coefficient of work function $d\phi/dT$ appears reasonably constant. Herring[17] pointed out four major contributions to $d\phi/dT$ that must be considered. They are (1) thermal expansions of the lattice, (2) effect of atomic vibrations on the internal electrostatic potential and (3) on chemical potential, and finally (4) the effect of electronic specific heat.

Inasmuch as effects (1) through (3) are not expected to lead to an alteration in sign with crystal direction,[17] one may interpret the appearance of both positive and negative values of $d\phi/dT$ as evidence for the importance of band-structure effects which may vary in sign. For example, it is interesting to speculate that large negative $d\phi/dT$ values observed along the ⟨100⟩, ⟨112⟩, and ⟨110⟩ directions may arise from nearly filled narrow $d$ bands along these directions.[28] Examination of the postulated electronic structure of tungsten[29] shows such possibilities exist along the ⟨110⟩ and ⟨100⟩ directions where nearly filled $d$ bands occur. Further theoretical study of these and other temperature effects on $\phi$ particularly as they relate to transition metals will be needed in order to fully understand their relative importance.

An additional contribution to the temperature de-

[28] N. Sun and W. Band, Proc. Cambridge Phil. Soc. **42**, 72 (1946).

[29] L. F. Mattheiss, Phys. Rev. **139**, 1893 (1965).

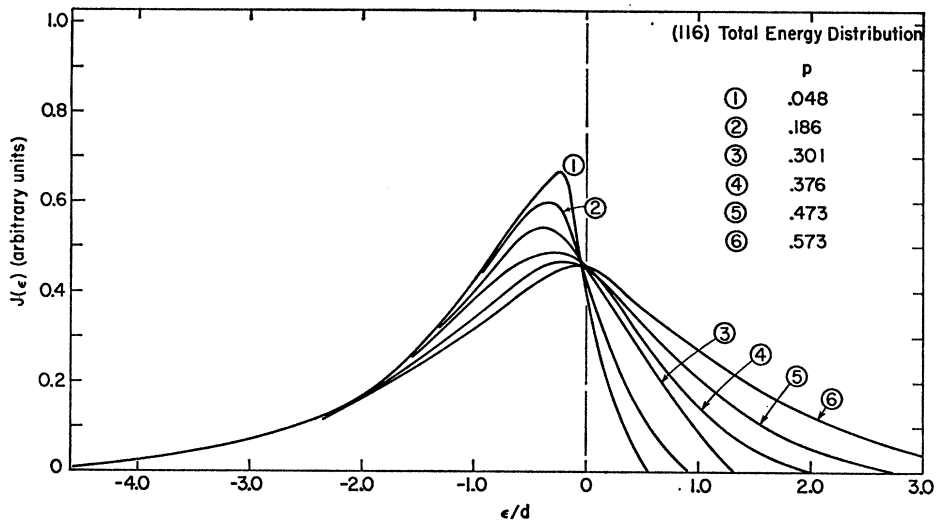


FIG. 12. Experimental total-energy-distribution plots along the ⟨116⟩ direction of a W emitter as a function of $p$, where $d=0.138$ eV and $F=3.04\times10^7$ V/cm.

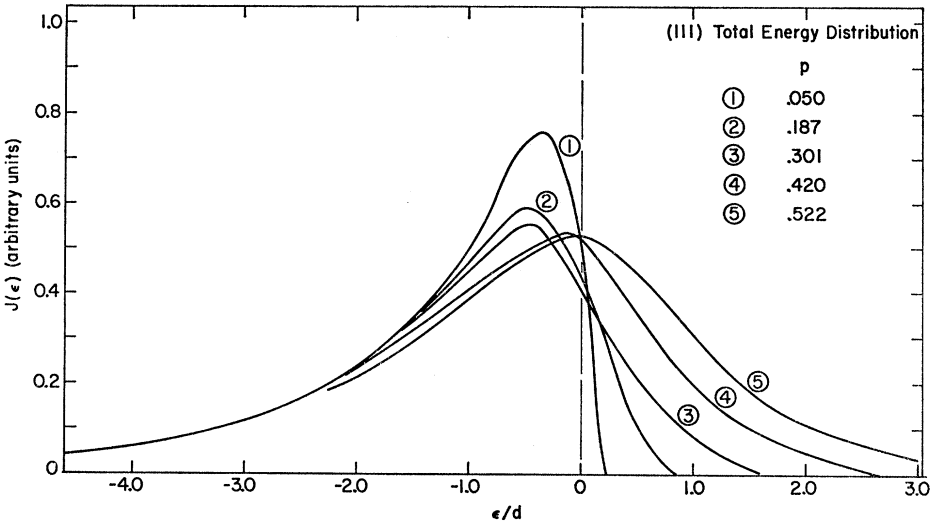


FIG. 13. Experimental total-energy-distribution plots along the ⟨111⟩ direction of a W emitter as a function of $p$, where $d=0.134$ eV and $F=2.99\times10^7$ V/cm.

rivative of $\phi$, considered by Herring to be only a fraction of $k$, was the temperature variation of the surface double layer $dD/dT$. For metal surfaces coated with adsorpates which greatly alter $D$, the value of $dD/dT$ is not negligible as shown for CsF coadsorbed on W,[30] where $d\bar{\phi}/dT=-2.4\times10^{-3}$ eV/deg, and as shown in Fig. 12 for ZrO coadsorbed on the 100 plane of W. For low $\phi$ surfaces the TF correction to the apparent work function becomes more significant and amounts to $\sim0.2$ eV at 650°K as shown in Fig. 8. Inasmuch as the ZrO layer nearly cancels out the clean W value of $d\phi/dT=-10.9\times10^{-5}$ eV/deg, we conclude that the ad layer possesses a dipole complex which diminishes in magnitude with temperature in contrast to CsF coadsorbed on W. Because Zr and O relative to Cs and F are closer in atomic size it is possible that the surface-field-erected dipole model may be more applicable to the ZrO system. According to Dykman[31] this model should exhibit a dipole moment which diminishes in strength with temperature as observed here for ZrO coadsorbed on the 100 plane of W.

## VI. CLEAN-TUNGSTEN ENERGY-DISTRIBUTION RESULTS

According to Eqs. (5) and (10), both the differential and integral forms of the current density vary exponentially with $\epsilon/d$ at low temperatures. We have shown that the variation of the integral field-emitted current with $\epsilon$ obeys Eq. (10) for five of the six crystallographic directions investigated This is rather compelling, although not sufficient, evidence that the Sommerfeld model is adequate for describing the emission along these directions. Except for the ⟨110⟩, the five crystal directions whose emission obeys Eq. (10) all give reason-

[30] L. W. Swanson *et al.*, Field Emission Corporation Final Report, Contract No. NASw-1082, 1966 (unpublished).

[31] I. M. Dykman, Ukrain Fiz. Zh. 1, 81 (1956).

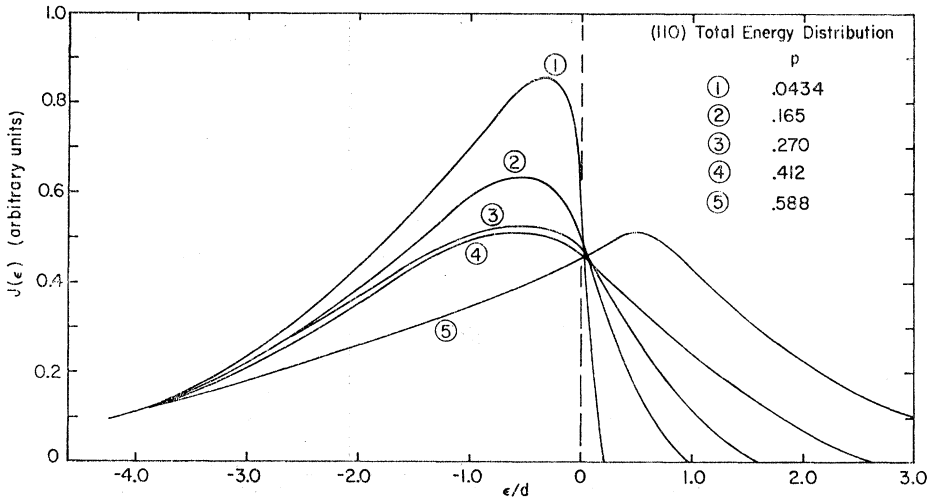


FIG. 14. Experimental total-energy-distribution plots along the ⟨110⟩ direction of a W emitter as a function of $p$, where $d=0.153$ eV and $F=3.70\times10^7$ V/cm.

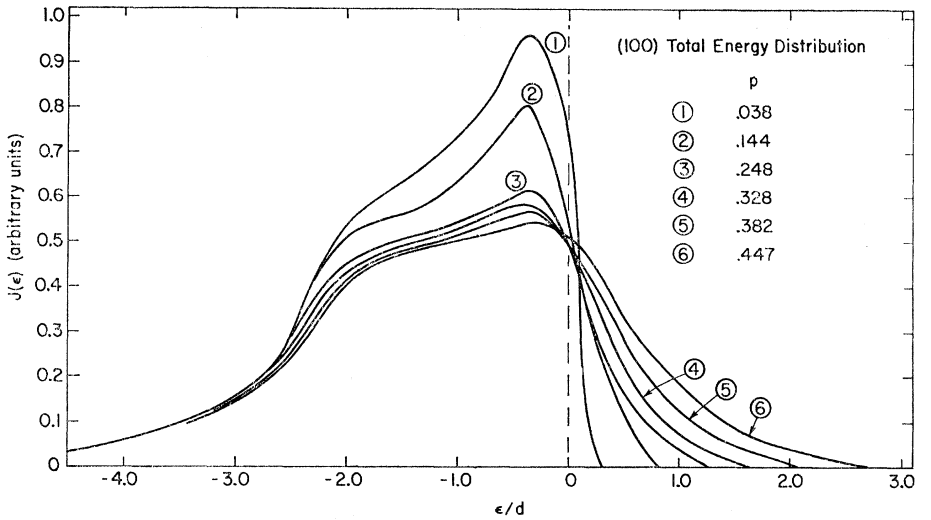


FIG. 15. Experimental total-energy-distribution plots along the ⟨100⟩ direction of a W emitter as a function of $p$, where $d=0.174$ eV and $F=4.08\times10^7$ V/cm.

able values of $\phi_e$, thus providing nearly unassailable proof for the adequacy of the Sommerfeld model for the ⟨310⟩, ⟨211⟩, ⟨111⟩, and ⟨611⟩ directions. In order to provide further experimental proof for these conclusions and further insight concerning the anomalies observed along the ⟨100⟩ and ⟨110⟩ directions, we have measured the total-energy distribution for each of these planes as a function of temperature. The determination of $d\phi/dT$ from the variation of the $I(V)$ characteristics with temperature, as described in the preceding section, hinges on the adequacy of the FN theory at elevated temperatures which can also be verified by total-energy-distribution measurements.

The total-energy-distribution curves $J(\epsilon)$ for six major crystallographic directions of W shown in Figs. 10–15 were obtained by graphical differentiation of the integral current according to the relation

$$J(\epsilon)=ndI_p/dV_t. \tag{20}$$

The normalization factor $n$ was adjusted for each plane to cause the experimental peak heights to match theory at $p=0.25$, and was further adjusted slightly with temperature to cause coincidence of the trailing edges at large $-\epsilon/d$ with the 77°K curve. The latter adjustment was necessitated by the temperature dependence of work function which alters $d$ in the function $\exp(\epsilon/d)$, which in turn controls the decay of $J(\epsilon)$ with $-\epsilon$. The temperature range is given in terms of the nondimensional parameter $p=kT/d$ and extends approximately from 77 to 900°K for each plane investigated. By plotting the abscissa as $\epsilon/d$, the shape of the respective curves can be compared directly with the corresponding theoretical curves of Fig. 1.

Because each of the energy-distribution curves in Figs. 10–15 was obtained from a ⟨100⟩-oriented emitter, except for the (110) results which were obtained from a ⟨310⟩-oriented emitter, the rather large angles of deflection resulted in values of $\phi_e$ that were much larger than the Table I results for the ⟨112⟩, ⟨110⟩, and ⟨111⟩ directions. Hence, the value of $d$ was evaluated from

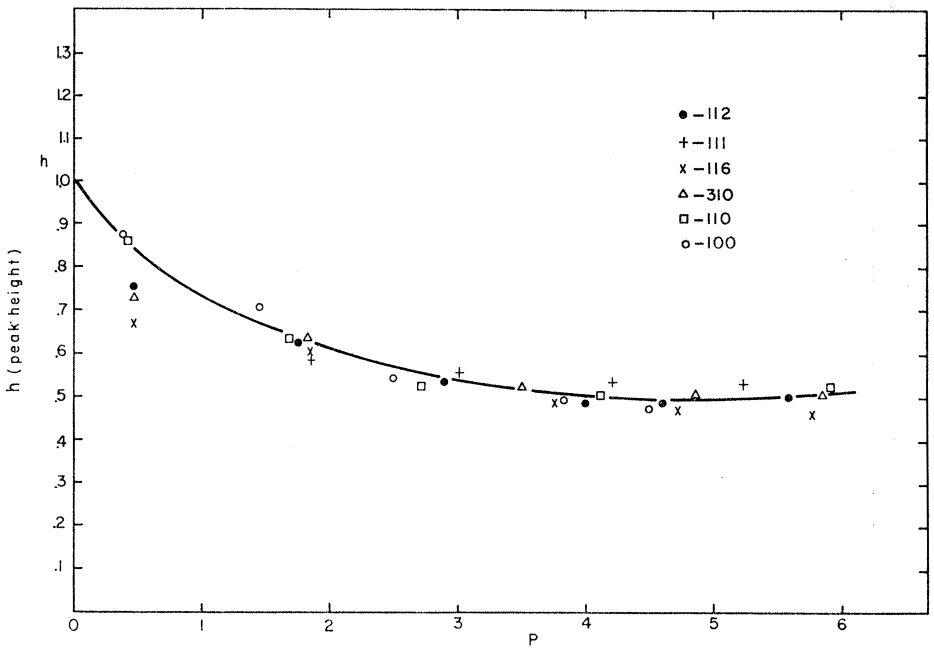


FIG. 16. Variation of relative peak height $h$ of the experimental energy-distribution curves as a function of $p$. Solid line based on free-electron mode [Eq. (5)].

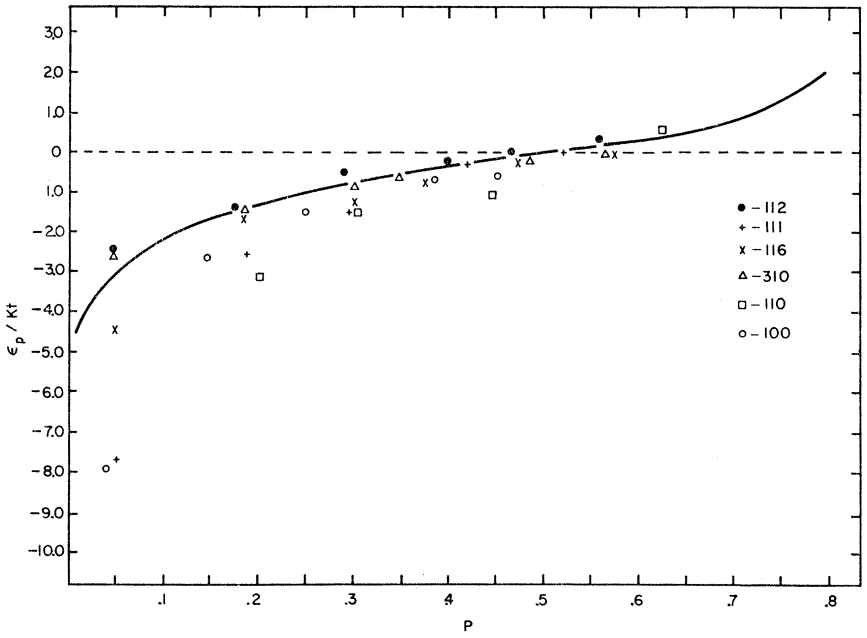


FIG. 17. Experimentally observed variation of the position of the energy-distribution peak relative to the Fermi level $\epsilon_p$ as a function of $p$. Solid line based on free-electron model [Eq. (5)].

Eq. (3) using measured values of $\phi_f$ and $F=\tilde{\beta}(\theta)V$. As mentioned previously, the electron optical effect caused by beam deflection increased the calculated value of $\phi_e$ due to a smaller measured value of $m_e$. The net effect of this artifact of the analyzer tube on the curves shown in Figs. 10–15 was to cause an apparent increase in the half-width measurement $\Delta$ of the energy-distribution curves. An additional increase in $\Delta$ occurred in the lower temperature range where the sharp peaks in the energy-distribution curves exceeded the resolution limitations of the analyzer.

A cursory examination of the energy-distribution curves of Figs. 10–15 reveals general agreement with the theoretical expectations of Fig. 1 for all but the ⟨100⟩ curve. The latter shows an anomalous broad shoulder approximately $2d\cong 0.35$ eV below $E_f$ on the trailing edge of the distribution. This special behavior for the ⟨100⟩ direction has been observed on both ⟨100⟩- and ⟨310⟩-oriented emitters. In addition, two different collector electrode surfaces provided identical results for all directions including the ⟨100⟩ direction. Thus, the anomalies of the observed ⟨100⟩ results cannot

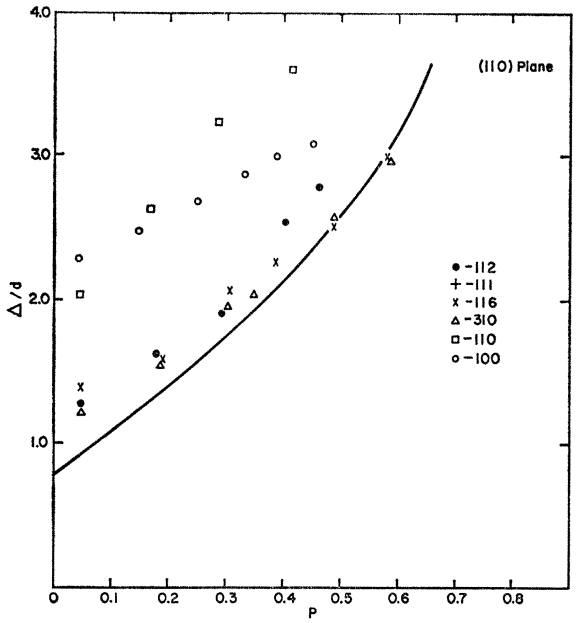


FIG. 18. Experimental normalized half-widths $\Delta/d$ of the total-energy-distribution curves plotted as a function of $p$. Solid line based on free-electron model [Eq. (5)].

be attributed to artifacts due to electron optical effects, magnetic field interactions, or collector patch-field effects. It should be mentioned that the direction of emission must coincide almost exactly with the ⟨100⟩ in order to observe the special distribution given in Fig. 15. For example, Fig. 12 shows nearly complete agreement with Eq. (5) for the ⟨611⟩ direction which is only 13° from the ⟨100⟩ direction.

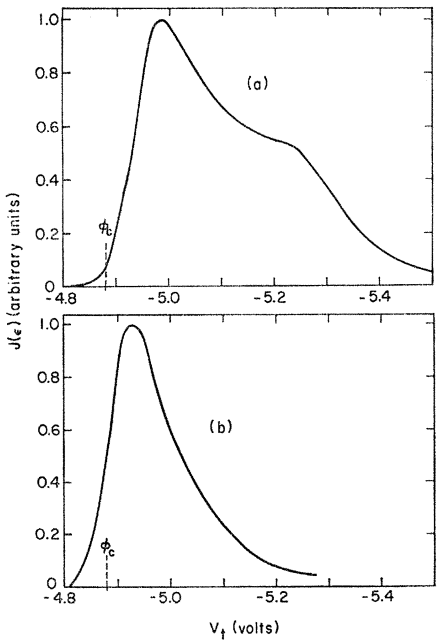


FIG. 19. (a) Curve shows the total-energy distribution from the ⟨100⟩ direction of a W emitter where $d=0.140$ eV and the anode voltage is 1235 V. (b) Curve shows the total-energy distribution from the ⟨100⟩ direction of a Zr-O-coated $W$ emitter where $d=0.091$ eV and the anode voltage is 767 V.

In order to illustrate more clearly some of the pertinent features of the energy-distribution curves a comparison is made in Figs. 16–18 between the variation of the peak height $h$, the position of the peak $\epsilon_p$ on the energy axis relative to the Fermi level and the value of $\Delta$ with the parameter $p$, and the theoretical predictions of the free-electron model depicted in Fig. 1. The variables $\epsilon_p$ and $\Delta$ were made dimensionless by dividing by $kT$ and $d$, respectively. Notice that variations of $\epsilon_p/kT$ and $h$ with $p$ are in close agreement with theory for all crystallographic directions, including the ⟨100⟩. The larger deviations from theory at the lowest values of $p$ are due to the resolution limitations of the analyzer, which become more apparent at low $p$ as expected. The good agreement at low values of $p$ for the ⟨100⟩ direction is somewhat surprising in view of the apparent non-free-electron behavior; however, since these data were obtained from a ⟨100⟩-oriented emitter, the resolution of the analyzer should be best for the (100) data. This suggests that the variations of $h$ and $\epsilon_p$ with $p$ for the ⟨100⟩ direction, which arise mainly from the Fermi-Dirac distribution term $[1+\exp(\epsilon/pd)]^{-1}$ in Eq. (5), are not affected by the apparent inadequacy of the Sommerfeld model exhibited below the Fermi level.

Although the variation of $\Delta/d$ with $p$ is in general agreement with Eq. (5) for the ⟨611⟩, ⟨111⟩, ⟨310⟩, and ⟨211⟩ directions, except at low values of $p$ where the resolution limitations of the analyzer become more important, the absolute values of $\Delta$ appear to be consistently too large. This is most likely due to the electron optical effects which, as mentioned, tend to decrease the rate of diminution of the term $\exp(\epsilon/d)$ with $-\epsilon$ and, hence, increase the apparent value of $\Delta$. At the largest values of $p$ additional uncertainty occurs due to excessive flicker noise which made accurate differentiation of the $I_p$-versus-$V_t$ curve somewhat difficult. We therefore view these results as confirming the expected variation of $\Delta/d$ with $p$ within the over-all uncertainty of the measurements.

On the other hand, the variation of $\Delta/d$ with $p$ for the ⟨100⟩ and ⟨110⟩ directions and particularly their absolute values are clearly not in accord with free-electron theory. In the case of the ⟨100⟩ direction the disagreement with theory is clearly due to the hump in the Fig. 19 results occurring 0.35 eV below $E_f$. The large value of $\Delta/d$ for the (110) results does not stem from a disagreement with the exponential decay law but rather from the unexpectedly small value of $m_e$, which was also responsible for the unusually large calculated values of $\phi_e$ relative to $\phi_f$ for the ⟨110⟩ direction noted in Sec. IV.

TABLE IV. Results from Zr-O-coated tungsten emitter (⟨310⟩ oriented).

| Plane | $V$ (V) | $d$ (eV) | $\phi_e$ (eV) | $\phi_f$ (eV) | $\bar{\phi}_f$ (eV) | $\beta/\bar{\beta}(\theta)$ | $M\times10^{-5}$ | $\theta$ (deg) |
|---|---|---|---|---|---|---|---|---|
| 100 | 767 | 0.091 | 2.28±0.03 | 2.84±0.03 | 3.00±0.05 | 0.72 | 6.2 | 18 |
| 310 | 1073 | 0.137 | 3.63±0.04 | 3.62±0.13 | 3.12±0.05 | 1.00 | 18.2 | 0 |

## VII. EFFECT OF COABSORBED ZIRCONIUM OXYGEN ON THE EMISSION CHARACTERISTICS OF W

Investigation of the emission characteristics of Zr-O coadsorbed on a W emitter was performed by coating a ⟨310⟩-oriented emitter from a suitable source. The striking alteration of the emission distribution upon coating with Zr-O has been discussed elsewhere.[9] The value of $\Delta$ at $p=0$ can be readily obtained from Eq. (5) and is given by

$$\Delta\cong0.69d. \tag{21}$$

At a constant current density, $\phi^{3/2}/F\cong$const, which, when combined with Eq. (21), yields

$$\Delta\cong\text{const}\phi. \tag{22}$$

Figure 19, showing the experimental energy-distribution results obtained from the ⟨100⟩ direction of a clean and Zr-O-coated W emitter, clearly indicates a reduction in $\Delta$; moreover, the energy distribution from the coated surface does not exhibit the anomalous hump shown in the clean W results. This is apparently due to the near-zero value of $J(\epsilon)$ in the energy range where the anomaly occurs on clean W. Table IV gives the values of $\phi_e$, $M$, and $\beta/\bar{\beta}(\theta)$ obtained from the ⟨100⟩ and ⟨310⟩ directions, while Fig. 20 shows a plot of the $I_p(V_t)$ data from the low-work-function emitter according to Eq. (10). The large increase in $M$ for both the ⟨310⟩ and ⟨100⟩ directions upon coadsorption of ZrO is indicative of a significant rearrangement of the substrate geometry. The localization of the work function changed to the (100) plane upon adsorption is apparent by noting that its work function is decreased from its clean value by 2.4 eV, whereas the (310) work function is diminished only 0.34 eV. This large anisotropy in work function should lead to a patch-field correction which, according to Young's formulation,[16] will reduce $\phi_f$ and $\phi_e$ in Table IV for the ⟨100⟩ direction. In view of the large uncertainty in the size of the low-work-function region, no patch-field correction has been attempted. However, the uncorrected values of both $\phi_e$ and $\phi_f$ are unusually low (considering that the ZrOW layer has already reduced the work function compared to a ZrW layer by ~1 eV) and application of patch-field corrections would further reduce these values.

In spite of the large increase in $M$ (compared with Table I results) upon Zr-O adsorption, the value of $\beta/\bar{\beta}(\theta)<1$ for the (100) plane suggests a faceted region. Examination of this system by field-ion microscopy[32] has revealed a geometrical perturbation of the surface which increased the net-plane step height and size in the (100) region. In the vicinals of the (100) plane a rapid change in the curvature occurs due to the termination of net-plane edges. Since a local change in $M$ arises from the integral effects of surface geometry, it is possible that the central regions of the (100) plane may possess an increased value of $M$ as well as a lower than average $\beta$ because of the large net planes along the ⟨100⟩. It also follows from Shrednick's observations[32] that proceeding from the ⟨100⟩ to the ⟨310⟩ direction should result in the observed increase in both $\beta$ and $M$ because of the rapid termination of net-plane edges. Thus, we conclude that information concerning geometrical changes in the surface can be ascertained from combined probe work-function and energy-distribution measurements.

Because of the anomalous energy distribution from the ⟨100⟩ direction, one may question the validity of the 2.28-eV work function obtained from Eq. (13) even though the fit of the data to Eq. (10) is adequate. In an attempt to ascertain the correctness of this value of $\phi_e$, the variation of the energy distribution with temperature was measured and plotted in Fig. 21. The values of $\phi$ obtained both by Eqs. (12) and (13) were used to calculate $p$. Inasmuch as values of $p=0.5$ according to theory should exhibit a symmetrical energy distribution, it was possible to determine the correct value of $p$ and, hence, $\phi$. Accordingly, as shown in Fig. 21, where the lower values of $\phi_e=2.28$ eV and

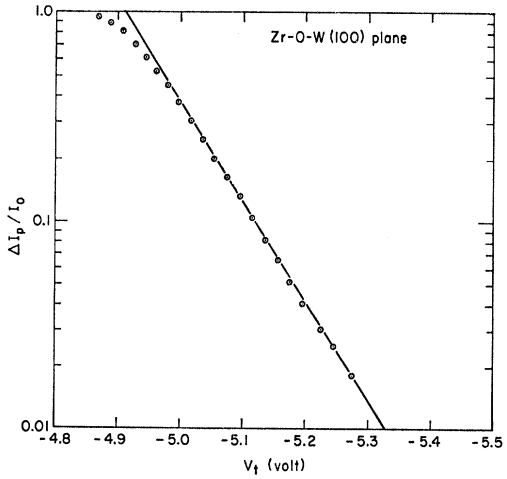


FIG. 20. Integral emitted current from the ⟨100⟩ direction of a circonium-oxygen-coated W emitter plotted according to Eq. (10). The anode voltage was 767 V and $d=0.091$ eV.

[32] V. N. Shrednick, Fiz. Tverd. Tela 3, 1750 (1961) [English transl.: Soviet Phys.—Solid State 3, 1268 (1961)].

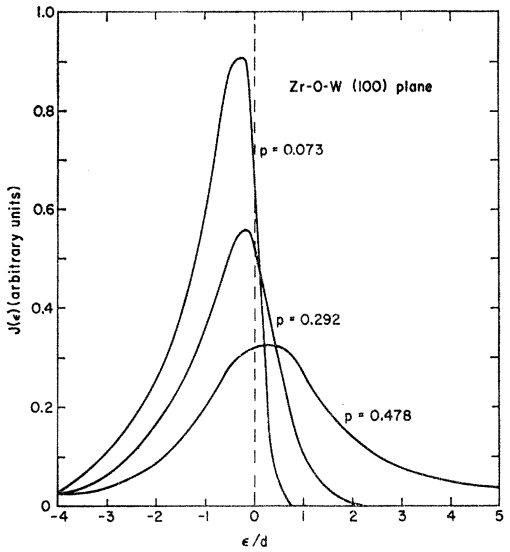


FIG. 21. Curves show the total-energy distribution from the ⟨100⟩ direction of a Zr-O-coated $W$ emitter at the indicated values of $p$. The anode voltage was 767 V and $d=0.091$ eV.

$\beta/\bar{\beta}(\theta)=0.72$ were employed, a correct value of $p=0.48$ occurs at the near symmetrical distribution, whereas the Fowler-Nordheim slope work function $\phi_f=2.84$ eV with $\beta/\bar{\beta}=1$ yields $p=0.38$. This internal self-consistency therefore lends support to the Table IV values of $\phi_e$ and $\beta$ obtained for the (100) plane coadsorbed with ZrO.

In order to further compare the energy-distribution results with theory, plots of $\Delta/d$ and $\epsilon_p/kT$ as a function of $p$ are given in Figs. 22 and 23. From the over-all agreement of the data with theory for the respective curves, one may conclude that the energy-distribution theory based on Eq. (5) is upheld along the ⟨100⟩ direction when a low work-function adsorbate such as coadsorbed Zr-O is present.

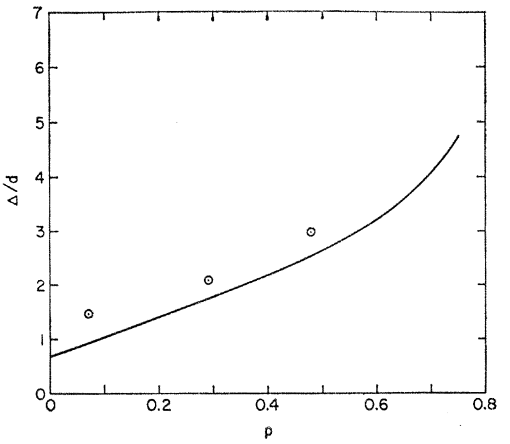


FIG. 22. Data points show the variation of the normalized half-width of the total-energy distribution with $p$ for the ⟨100⟩ direction of a Zr-O-coated W emitter, where $d=0.091$ eV. Solid line is the theoretical curve based on a free-electron model [Eq. (5)].

## VIII. BAND-STRUCTURE EFFECTS

The theoretical considerations of the total-energy distribution of field-emitted electrons from metals given earlier suggest that, except for Fermi surfaces of small radii of curvature or small electronic mass in the case of spherical surfaces, free-electron theory [i.e., Eq. (5)] is adequate. The results reported here generally support this picture for clean W along the ⟨116⟩, ⟨112⟩, ⟨111⟩, and ⟨130⟩ directions. It should be emphasized, however, that agreement of the experimental energy-distribution results with Eq. (5) does not necessarily substantiate the Sommerfeld model for the metal. Agreement with theory basically implies that the radius of curvature of the Fermi surface, i.e., the maximum value of $E_t$ for a given range of $\phi_p$ and $E$ along a particular direction, is sufficiently large that the band-structure term of Eq. (1) is unity. It is interesting to speculate that the hump occurring 0.35 eV below the Fermi energy in the energy-distribution curve along the ⟨100⟩ direction is due to band-structure effects.

Examination of the possibility of band-structure effects on the clean W results requires a brief review of the current picture of the electronic structure of W. From a variety of electronic and solid-state measurements[33–37] and theoretical analyses[29,38] of group VI metals, and more particularly W, it is now apparent that free-electron behavior is neither manifested nor expected. Figure 24 shows the expected band structure of W along several major crystallographic directions based on theoretical compilations by Mattheis.[29] The notation of Bouckaret, Smoluchowski, and Wigner[39] is employed and Fig. 25 shows the first Brillouin zone of the bcc

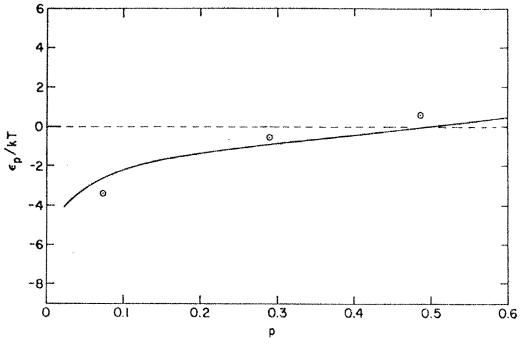


FIG. 23. Data points show the variation of the position of the energy-distribution peak relative to the Fermi level $\epsilon_p$ with $p$ for the ⟨100⟩ direction of a Zr-O-coated W emitter, where $d=0.091$ eV. Solid line is the theoretical curve based on a free-electron model [Eq. (5)].

[33] E. Fawcett and D. Griffith, J. Phys. Chem. Solids **23**, 1631 (1962).
[34] E. Fawcett and W. A. Reed, Phys. Rev. **134**, A723 (1964).
[35] J. A. Rayne, Phys. Rev. **133**, A1104 (1964).
[36] G. B. Brandt and J. A. Rayne, Phys. Rev. **132**, 1945 (1963).
[37] W. M. Walsh, Jr., and C. C. Grimes, Phys. Rev. Letters **13**, 523 (1964).
[38] T. L. Loucks, Phys. Rev. **143**, 506 (1966).
[39] L. Bouckaret, R. Smoluckowski, and E. Wigner, Phys. Rev. **50**, 58 (1936).

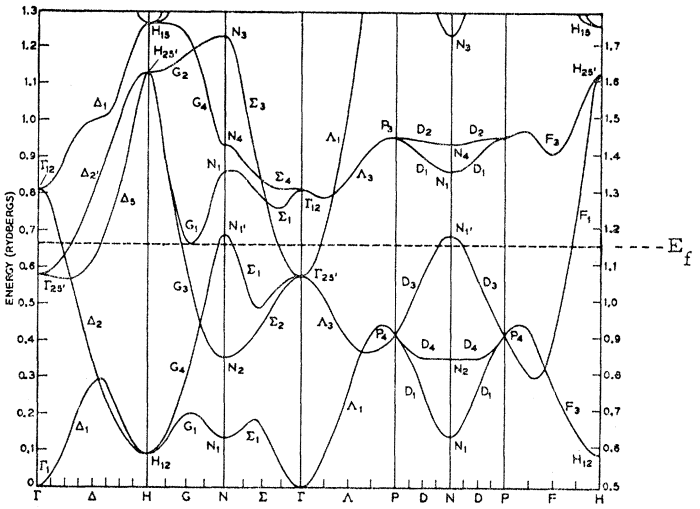


FIG. 24. Energy bands $E(\mathbf{k})$ along symmetry directions in the Brillouin zone for tungsten obtained from Ref. 29.

structure with the corresponding labeling scheme. The point at which the Fermi level intersects the band along the various directions defines the Fermi surface in $\mathbf{k}$ space. Several important features of the Fermi surface for W have now been established. Most interesting of these is an octahedral "jack-like" electron Fermi surface centered on the origin of the Brillouin zone $\Gamma$, pointed along the six $\langle 100\rangle$ directions ($\bar{\Gamma}\bar{H}$) and separated from a similarly shaped hole octahedron at symmetry point $H$ by small "ball-like" protrusions of electron surface also centered on the $\bar{\Gamma}\bar{H}$ axis; depending on the degree of spin-orbit coupling the ball-like protrusions along $\bar{\Gamma}\bar{H}$ may also contain smaller "lens-shaped" electron surfaces.[29] In addition, a smaller nearly spherical hole surface is expected to occur along the $\langle 110\rangle$ directions centered on symmetry points $N$. Cross sections of the Fermi surface of W without spin-orbit or relativistic corrections are reproduced in Fig. 26. Relativistic or spin-orbit coupling corrections yield a band structure along the $\bar{\Gamma}\bar{H}$ direction as shown in Fig. 27 (these figures taken from Ref. 38). The primary features of spin-orbit and relativistic corrections[38] are the disappearance of the electron lens, a separation between the electron and hole surface along $\bar{\Gamma}\bar{H}$, and a disappearance of the hole surfaces at $N$. Experimental results,[40] however, show the retention of a small ($E_f=0.284$ eV, measured from the band maxima) ellipsoidal hole surface at $N$.

The observed anomaly in the experimental $\langle 100\rangle$ energy distribution suggests the possibility of unusually small closed energy surfaces near $E_f$ along the $\bar{\Gamma}\bar{H}$ direction. In order to provide a quantitative basis for this possibility, it is necessary to solve the integral in the band-structure term

$$g=\left[1-\frac{1}{2\pi}\int_0^{2\pi}\exp(-E_m/d)d\phi_p\right]$$

for the various constant-energy surfaces contributing to the emission. At the present time the complexities of the proposed shapes of the energy surfaces and uncertainties as to the magnitude and variation of $E_m$ with $\epsilon$ preclude quantitative evaluation of this term. However, certain qualitative features of the energy-surface structure can be ascertained from the variation of the band-structure term and, more specifically, $E_m$ required to account for the results shown in Fig. 15.

If we take the hump in the $\langle 100\rangle$ energy distributions to represent excess current, it is clear that the value $J_h(\epsilon)$ for the surface contributing to the "hump" emission is zero at $E_f$; that is to say $g\sim 0$ for the $J_h(\epsilon)$ emission until $\epsilon\lesssim -0.3$ eV at which point emission from an additional energy surface $J_h(\epsilon)$ must occur. In order that $J_h(\epsilon)$ contribute significantly, its value of $E_m$ must be sufficiently small so that for a given value of $\epsilon$ the normal energy $E_x$ is large along $\bar{\Gamma}\bar{H}$ and small along all other directions. As $\epsilon$ decreases, $E_m$ apparently increases, thereby causing $g$ and hence $J_h(\epsilon)$ to increase; further decrease in $\epsilon$ below $\sim -0.4$ eV causes a sharp drop in $J_h(\epsilon)$ according to Fig. 15, which may be due to a decreasing value of $E_m$ and/or to the rapidly diminishing value of $\exp(\epsilon/d)$ with decreasing negative $\epsilon$. The contention that the energy surfaces emitting at $E_f$ are normal (i.e., $E_m \gg d$) is attested to by the apparent Sommerfeld behavior along the $\langle 100\rangle$ when the low work-function ZrO layer is present and emission is mainly confined to the top of the conduction band. The normal behavior of $h$ and $\epsilon_p$ for the $\langle 100\rangle$ results is

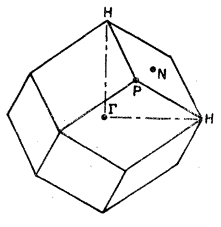


FIG. 25. First Brillouin zone of a body-centered cubic structure. Letters indicate directions of reciprocal lattice space used in Fig. 24.

[40] D. M. Sparlin and J. A. Marcus, Phys. Rev. 144, 484 (1966).

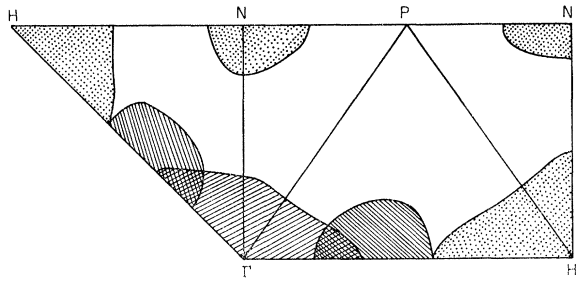


FIG. 26. Nonrelativistic Fermi surface of tungsten according to Loucks (Ref. 38).

further evidence that emission near the top of the band obeys Eq. (5). Additional confirmation that the energy surface contributing to $J_h(\epsilon)$ is small and centered along the $\bar{\Gamma}\bar{H}$ axis stems from the fact that the ⟨116⟩ direction, which is only 13° from the ⟨100⟩, yields an energy distribution in complete agreement with Eq. (5).

It is conceivable that the small energy surface centered along $\bar{\Gamma}\bar{H}$ which contributes to $J_h(\epsilon)$ stems from the small hump in the $\Delta_7$ band approximately 0.4 eV below $E_f$ as shown in Fig. 27 where spin-orbit coupling corrections are included. Also, as observed from Fig. 27 the Sommerfeld behavior near $E_f$ along $\bar{\Gamma}\bar{H}$ is not unexpected in view of the fact that the Fermi surface appears sufficiently large to satisfy the condition $E_m \gg d$.

A final comment should be made concerning the possible influence of the two hole surfaces—a small ellipsoidal hole surface located at $N$ and a large octahedral-shaped surface centered on $H$—on the energy distribution results. Treating theoretically the emission from a valence band, Stratton[12] obtains a general expression for the energy distribution similar to that of conduction-band emission, i.e., Eq. (1). As in the case of conduction-band emission the major contribution to $J(\epsilon)$ again comes from electrons with small values of $E_m$. Stratton also finds that values of $\Delta$ for valence-band emission are larger than conduction-band emission for corresponding values of $p$.

In the case of W, one must consider the effect of the hole surfaces centered on the $\bar{\Gamma}\bar{N}$ and $\bar{\Gamma}\bar{H}$ axes on the electron emission along the ⟨110⟩ and ⟨100⟩ directions. In view of the large $E_m$ values associated with the hole surfaces at $H$ for emission along the ⟨100⟩ direction when compared with the much smaller values of $E_m$ for the hole surfaces at $N$ for ⟨110⟩ direction emission (see Ref. 40), one expects a significant contribution to the respective emission directions from only the latter hole surface. Thus, along the ⟨110⟩ direction each of the two overlapping electron and hole bands contribute to the total emission; the larger value of $\Delta$ for emission from the nearly filled band at $N$ may therefore predominate in the observed exponential tail of the energy distribution to give the anomalously large values of $\Delta$ as shown in Fig. 18 for the ⟨110⟩ direction and contribute in part to the discrepancy between $\phi_e$ and $\phi_f$.

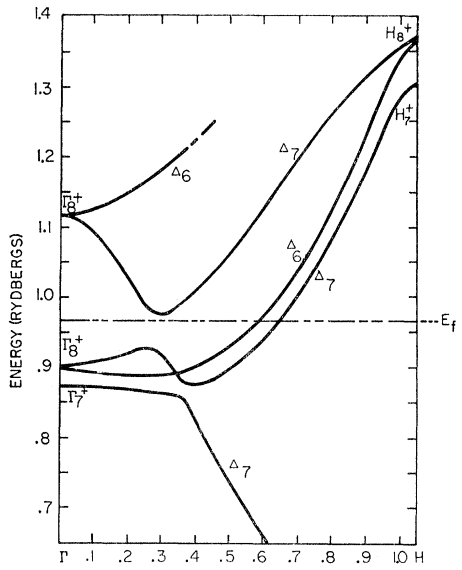


FIG. 27. Energy bands for tungsten along $\Gamma H$ with relativistic corrections according to Loucks (Ref. 38).

It should be mentioned that the degree of correlation between the energy-surface shapes inferred from bulk electronic measurements and energy-distribution results is not completely clear. This uncertainty arises from the unknown influence of the nearby physical surface on the interatomic potentials and, hence, on the band structure along a specific direction normal to the surface. However, the degree of correlation with bulk expectations suggested by our interpretations indicates bulk band structure is not greatly altered near the physical surface. The results with coadsorbed ZrO also provide evidence that adsorbed surface layers only affect the energy distributions curves through the variation of $d$ due to changes in work function and applied electric field.

## IX. CONCLUSION

We have shown that the absolute values of $\phi$, $\beta$, and $M$ can be obtained from combined energy-distribution and Fowler-Nordheim results for those emission directions obeying Eq. (5), thereby providing important insight into the electronic and geometric nature of the clean and Zr-O-coated surface of W. Also, the temperature dependence of $\phi$ is shown to vary both in sign and magnitude with crystal direction, thus providing an interesting basis for further theoretical study of the relative importance of thermal effects on the inner and outer parts of the work function.

The total-energy-distribution results clearly indicate that the Sommerfeld-model description of field emission from W, and conceivably from other transition metals, must be used with caution since it is clearly inadequate for the ⟨100⟩ and possibly the ⟨110⟩ directions. Our measured energy-distribution results are in accord with

expectations based on theoretical band-structure calculations for W by Mattheiss[29] and Loucks[38]; namely, the Sommerfeld model for field emission is adequate along those directions for which constant energy surfaces at or near $E_f$ intersect broad, partially filled bands; on the other hand, those directions which possess narrow, nearly filled $d$ bands or bands that cross within a few times $d$ below $E_f$, as is the case shown in Fig. 24 for the ⟨110⟩ and ⟨100⟩ directions of clean W, are accordingly found to exhibit certain anomalies in their energy-distribution results. Thus it appears that total-energy-distribution measurements can be a new and useful tool for analyzing certain characteristics of energy surfaces near $E_f$ for metals and semiconductors.

## ACKNOWLEDGMENTS

The authors wish to thank Headquarters, National Aeronautics and Space Administration, Washington, D.C., for their support of this work. We are also grateful to Dr. F. M. Charbonnier for many helpful discussions and to Dr. W. P. Dyke for his continued interest in this work.

PHYSICAL REVIEW VOLUME 163, NUMBER 3 15 NOVEMBER 1967

# Activity-Coefficient and Vacancy Flow Effects on Tracer Diffusion Coefficients in Silver-Gold Alloys*

R. O. MEYER
*University of Arizona, Tucson, Arizona*
(Received 18 May 1967)

In work reported previously, measurements of silver and gold tracer activities were made in silver-gold-alloy Kirkendall diffusion couples in which the tracers were originally placed in the interface. Semilogarithmic plots of these data were straight lines, but the coefficients measured were not self-diffusion coefficients because of the effects of the composition gradient. These straight-line graphs are now explained, and an approximate equation for the diffusion coefficients is derived from the theory reported earlier. Some of the measured values disagree with the calculation and the disagreement is outside of the estimated errors.

## I. INTRODUCTION

IN a previous paper,[1] the mean atom drift was measured for radioactive gold and silver tracers placed at the interface of silver-gold-alloy Kirkendall diffusion couples. After a diffusion anneal, the tracer distribution resembled a Gaussian and plots of logarithm of specific activity versus the square of the distance from the center were straight lines, except near the center. In the present paper, an approximate equation is developed for the diffusion coefficients which result from these straight lines, and coefficients from this earlier data are compared with the calculated values.

TABLE I. Summary of notation.

| Symbol | Definition |
|---|---|
| $i$ | Ag or Au |
| $c_i^*$ | Tracer concentration (specific activity of $i$) |
| $N_i$ | Composition of couple (atom fraction of $i$) |
| $D_i^*$ | Self-diffusion coefficient of $i$ |
| $\gamma_i$ | Activity coefficient of $i$ |
| $w_i$ | Jump frequency of a type-$i$ atom |
| $W$ | $N_{Ag}w_{Ag}+N_{Au}w_{Au}$ |
| $f_i$ | Correlation factor for type-$i$ atom |
| $\alpha$ | Factor containing vacancy correlation effects ($\alpha=1.27$ here) |

* Work supported in part by the U. S. Atomic Energy Commission through Contract AT(11-1)-1041.

[1] R. O. Meyer and L. M. Slifkin, Phys. Rev. 149, 556 (1966).

## II. THEORY

From Eq. (1) and Eq. (4) of the earlier paper,[1] we can write down an equation for $v(x,t)$, the drift velocity of a tracer atom due to a composition gradient,

$$v(x,t)=D_i^*K(\partial N_i/\partial x)+v_R, \quad (1)$$

which is given relative to the inert interface markers. The quantity $K$ contains a number of terms depending on the activity coefficient $\gamma_i$ and self-diffusion coefficients $D_i^*$. The term containing $K$ is due to Le Claire[2]

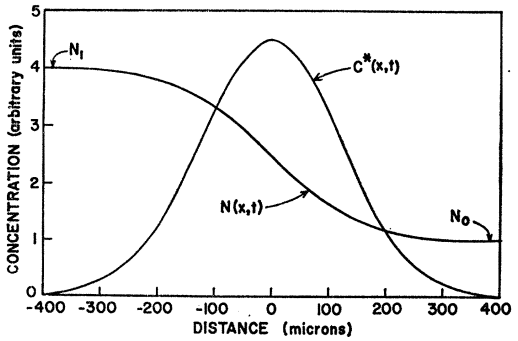


FIG. 1. Typical tracer and chemical concentrations.

[2] A. D. Le Claire, Phil. Mag. 3, 921 (1958).